Starvation response strategies of human gut bacteria *Bacteroides thetaiotaomicron* and *Roseburia intestinalis* and their impact on co-culture dynamics

Bin Liu*[1], Daniel Rios Garza*[1], Didier Gonze[2], Anna Krzynowek[1], Kenneth Simoens[3], Kristel Bernaerts[3], Annelies Geirnaert[4], Karoline Faust[1]

[1]Department of Microbiology, Immunology and Transplantation, Rega Institute for Medical Research, Laboratory of Molecular Bacteriology, KU Leuven, B-3000 Leuven, Belgium

[2]Unité de Chronobiologie Théorique, Faculté des Sciences, CP 231, Université Libre de Bruxelles, Bvd du Triomphe, 1050 Bruxelles, Belgium

[3]Department of Chemical Engineering, Chemical and Biochemical Reactor Engineering and Safety (CREaS), KU Leuven, B-3001 Leuven, Belgium

[4]Laboratory of Food Biotechnology, Department of Health Sciences and Technology, Institute of Food, Nutrition and Health, ETH Zürich, CH-8092 Zürich, Switzerland

* authors contributed equally

Abstract

We explore the impact of nutrient scarcity on the interaction dynamics of two common human gut bacteria, *Bacteroides thetaiotaomicron* (BT) and *Roseburia intestinalis* (RI). Upon depletion of glucose, the viable cell numbers of BT decrease, whereas RI enters a slow growth mode. When mucin beads are supplemented, both species attach to the beads and the number of viable BT but not RI cells in liquid increases significantly. In co-culture, viable cell numbers decrease or increase significantly compared to monoculture, depending on the time point. A combination of targeted metabolomics and RNA-seq showed that RI's slow growth mode represents a diauxic shift towards acetate and lactate consumption, whereas BT survives glucose depletion by foraging mucin sugars. Most tested mucin monosaccharides inhibit the growth of RI but not BT on glucose. We encoded our findings in a kinetic model, which qualitatively reproduces the observed dynamics.

Introduction

The human gut is populated by hundreds of microbial species interacting with each other and with the human host. Gut bacterial species differ in their distribution along the human digestive tract and favor different microhabitats, such as the lumen of the large intestine, colonic crypts and mucus layers[1,2]. Diverse growth rates and attachment properties of gut bacteria help establish spatially structured communities. Also, the spatially heterogeneous environment influences the colonization success of different members of the gut microbiota and their competitive or cooperative relationships with one another[3–8].

An efficient way to acquire nutrients is essential for microbial persistence in the human gut. In addition to dietary fiber in the lumen, host-derived mucin glycans provide an alternative source of nutrients for members of the gut microbiota[9]. The colonic mucus layer, located at the interface between the epithelium and the gut microbiota, is key to maintain intestinal homeostasis and to enhance the resilience to perturbations of the gut microbiome[10,11]. Mucus is continuously secreted by goblet cells and is organized into two distinct layers: an inner dense layer tightly attached to the epithelium, which appears to be essentially sterile when healthy; and an outer loose layer with an expanded volume, which supports a metabolically diverse community. The outer layer provides mucin polysaccharides and

50 serves as attachment sites for the gut species that co-evolved to utilize these substrates,
51 giving rise to complex microbial interactions[9,10,12,13]. *Bacteroides* is one of the most
52 abundant but also most variable genera across human fecal samples[14]. Its most studied
53 species *Bacteroides thetaiotaomicron* (BT) holds a large repertoire of genes involved in
54 sensing and hydrolyzing many different polysaccharides, and BT was reported to strongly
55 express genes involved in the degradation of dietary plant glycans[15,16]. As a nutritional
56 generalist, BT can alter its metabolic response to mucin glycans in the absence of dietary
57 nutrients, to colonize the mucus layer and maintain its persistence in the human gut[17].
58
59 Short-chain fatty acids (SCFAs) including acetate, propionate and butyrate, are the major
60 end products of the anaerobic fermentation of polysaccharides by the human gut
61 microbiota. All these SCFAs exert multiple health benefits, in particular butyrate, which is
62 used preferentially as an energy source to fuel colonic enterocytes and may trigger signals
63 regulating mucin synthesis and secretion[18,19]. Metabolic cross-feeding of the human gut
64 microbiota impacts SCFA production[20]. For example, members of the most abundant
65 genera, including *Faecalibacterium*, *Eubacterium* and *Roseburia*, are able to convert acetate
66 and/or lactate into butyrate using the prevalent butyryl-CoA:acetate CoA-transferase
67 pathway[21,22]. Lactate is also an important end product of anaerobic fermentation in the
68 gut[23]. In addition to acetate as a key intermediate that promotes cross-feeding interactions
69 of the gut microbiota, the role of lactate as substrate for butyrate producers may explain its
70 low levels of accumulation in the human colon of healthy adults[24,25]. Upon exhaustion of the
71 primary carbon sources such as carbohydrates in the gut, microbes have to hunt for another
72 carbon source to thrive. It was reported that acetate could promote the growth of a
73 common intestinal butyrate-producing species *Roseburia intestinalis* (RI) during growth on
74 glucose[26–28].
75
76 Several studies employing in vitro fermentation systems have shown mucin as a driving
77 force in forming a microbial community that is phylogenetically and metabolically distinct
78 from the luminal one[29,30]. 16S rRNA gene-based results of complex communities from an in
79 vitro gut model showed that RI colonized mucin-covered carriers[31]. For unclear reasons,
80 *Roseburia* but not *Bacteroides* decreased in relative abundance with mucin
81 supplementation[32]. We thus require a mechanistic understanding of how mucin formed

microhabitats impact the abundance of different gut species. Here, we built an in vitro batch system containing mucin beads, to systematically investigate how a spatially structured environment in the presence of mucin beads influences the growth and interactions of the model gut species BT and RI. The growth dynamics of monocultures and co-cultures in the liquid medium and attached to the beads were monitored using live/dead cell staining followed by flow cytometry in combination with machine learning techniques to quantify their proportions in co-culture. Subsequently, we characterized the effect of mucin degradation products on the abundance of BT and RI, and found that it depended on the sugar level being considered. Transcriptomic analyses of monoculture and co-culture in medium with and without mucin beads at several time points revealed different nutrient harvesting strategies employed by BT and RI, which resulted in their different growth modes, and also changed their interaction mechanisms depending on nutrient availability. We further developed a kinetic model that accounts for pH conditions, metabolites, and growth profiles, to mechanistically understand how gel-entrapped mucin influences the proliferation of BT and RI and the dynamics of their relationship.

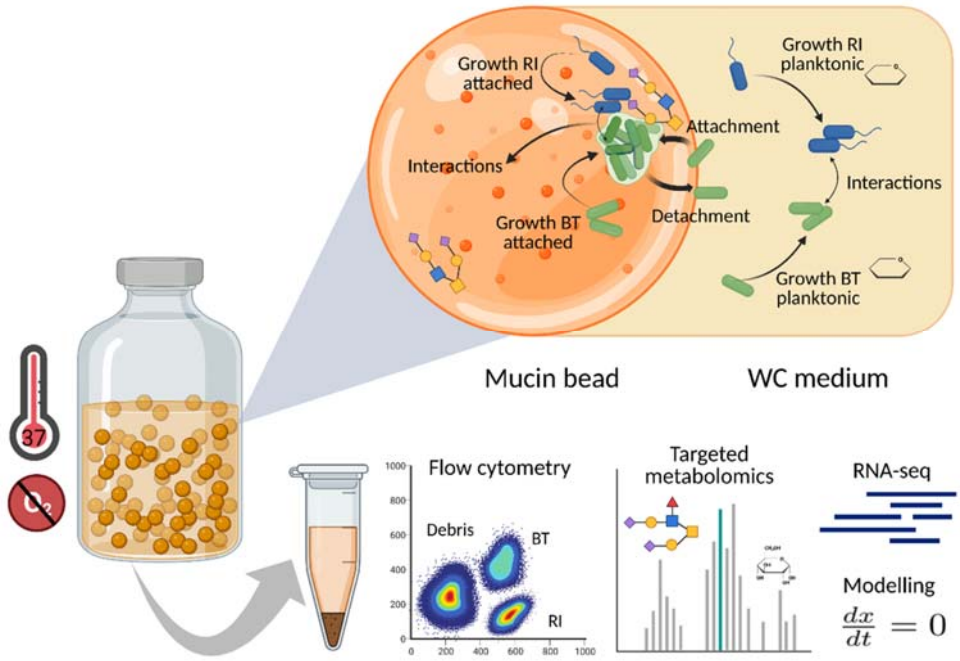

Figure 1. Experimental setup and design. We used a bottle system containing mucin beads in WC medium to mimic the spatially structured environment of the human gut. The growth dynamics of monoculture and co-culture in the liquid medium and attached to the beads

102 were monitored using flow cytometry with live/dead cell staining. Live cells of BT and RI
103 were differentiated from each other and from debris using a UMAP-based classification
104 strategy (details in the "Methods" section). Fermentation products, including short-chain
105 fatty acids and mucin-derived monomeric sugars, were measured by high-performance
106 liquid chromatography and gas chromatography. The presence and quantity of mRNA in
107 samples collected at different time points were assessed by RNA-seq. Further, a kinetic
108 model with ordinary differential equations was developed that summarizes our
109 understanding of the system. O_2: oxygen; WC: Wilkins Chalgren medium; BT: *Bacteroides*
110 *thetaiotaomicron*; RI: *Roseburia intestinalis*.
111

112 ## Results

113 **Different responses to sugar depletion**

114 Glucose and pyruvate were provided as the main carbon sources in WC (Wilkins Chalgren)
115 medium (Figure 2a). When grown in monoculture, BT produced succinate, lactate, formate,
116 and acetate during fermentation, which decreased the pH from 6.7 to 5.0. At 16 h, BT
117 reached its maximal density of 1.2×10^6 viable cells/µl. After the depletion of glucose and
118 pyruvate, the acidic conditions led to a loss of viable BT cells but did not affect the total cell
119 count. Loss of viability at low pH (5.0) was further confirmed by spent media and pH
120 experiments. We re-grew BT in its spent medium (collected at 48 h cultivation when glucose
121 is depleted), and found that an initial pH of 6.5 is required for growth (on trehalose; Figure
122 S1). Supplementing the spent medium with glucose and pyruvate only enhanced growth
123 when the pH was also increased (Figure S1a). In addition, BT did not grow on glucose and
124 pyruvate when the pH of WC medium was lowered to 4.5 and 5.0, respectively, and its
125 growth rate was decreased at pH 5.5 and 6.0 compared to pH 6.7 (Figure S1b). RI in
126 monoculture produced lactate, formate, acetate and butyrate from glucose and pyruvate,
127 corresponding to a pH decrease from 6.7 to 5.7 at 16 h and reached a maximal density of 7.8
128 $\times 10^5$ viable cells/µl (Figure 2b). After the depletion of glucose and pyruvate in 24 h, RI
129 gradually entered a slow growth mode, seen as a drop in viable cells to $1.8\text{-}3.8 \times 10^5$ cells/µl
130 from 40 h to 120 h in two independent experiments. In addition, we observed a further
131 significant ($P < 0.001$ by Student's t test) increase of butyrate concentration concurrent with
132 decreasing acetate and, in some cases, lactate (Figure 2b and Figure S2 for lactate

133 consumption in RI monoculture), resulting in a pH increase from 5.7 to 6.0. In brief, viable
134 BT cells decline primarily due to the lowered pH, whereas RI maintains higher cell densities
135 by entering a slow growth mode.
136
137 Given the observed diauxic shift from glucose/pyruvate to lactate/acetate, we performed
138 RNA-seq of RI grown in monoculture for several time points and replicates to investigate its
139 metabolic mechanism. During the exponential growth period, genes associated with
140 glycolytic and pyruvate-utilizing pathways were more highly expressed at mid-log phase of
141 12 h compared to at 4 h (Figure S3b). Interestingly, although glucose ran out at 48 h, we
142 found that RI kept expressing glycolysis genes and also non-essential genes such as those
143 involved in cell motility although growing in a well-mixed environment (Figure S4). We
144 further compared the effect of different normalization methods (transcripts per million and
145 DESeq2's median of ratios[33]). In general, both methods showed consistent results except for
146 some glycolysis genes, including hexokinase (HEX1; RIL182_00253) and phosphoglycerate
147 mutase (PGM; RIL182_01289) (Figure S5). We used a strict cutoff of at least 1.5-fold change
148 and a Benjamini-Hochberg adjusted *P* value less than or equal to 0.01 for differential
149 expression calculated by DESeq2. When comparing the transcript levels of RI in monoculture
150 between 12 h and 48 h, the significant up-regulation of genes encoding lactate
151 dehydrogenase (RIL182_00335 and 01719) and butyryl-CoA:acetate CoA-transferase
152 (RIL182_00413) corroborates the finding that RI converts lactate/acetate to butyrate after
153 glucose depletion. The energy yielded by butyrate production from lactate/acetate ($\Delta_f G^0$ = -
154 46 KJ/mol) is much lower than that from glucose ($\Delta_f G^0$ = -250 KJ/mol)[34]. Therefore, it is not
155 surprising that RI grows more slowly on lactate/acetate. In summary, RI maintains its slow
156 growth in the absence of glucose by converting acetate and lactate to butyrate.
157
158 **Effects of mucin on monoculture**
159 BT survives longer in the presence of mucin beads than without them. After depleting
160 glucose and pyruvate at 24 h, BT in liquid retained a viable cell count higher than 1.0×10^6
161 cells/µl (Figure 2d). We further extended the cultivation period with mucin beads from 120
162 h to 288 h and observed a consistently stable population of BT in the liquid broth (Figure
163 S6). In addition, the growth of RI on glucose/pyruvate seems to be impeded by mucin,
164 demonstrated by a longer lag phase of 12 h and lower maximum of 4.5×10^5 viable cells/µl

165 at 36 h when compared with RI grown in WC without mucin beads (Figure 2e). After nutrient
166 depletion, RI still exhibited the slow growth mode characterized by a further increase of
167 butyrate and decrease of lactate/acetate, but with a much lower density of 0.3-0.5 × 10^5
168 viable cells/μl than in the absence of mucin. In addition to the planktonic cells in liquid, we
169 also quantified the cells of BT and RI attached to the mucin beads at different time points.
170 As shown in Figure 2d and 2e, attached BT and RI in monoculture reached maximal densities
171 of 6.0 × 10^5 viable cells/μl at 24 h and 1.1 × 10^5 viable cells/μl at 32 h, respectively. Thus, in
172 the presence of mucin, BT can maintain high densities in the long term, whereas the density
173 of RI declines.
174
175 Regarding the mucin degradation products, the concentration of *N*-Acetylneuraminic acid
176 (Neu5Ac) showed a significant ($P < 0.001$ by Student's t test) increase of 0.12 mM in BT
177 monoculture after 120 h and no significant change in RI monoculture (Figure 2d-e). We also
178 observed higher levels of fucose and galactose for BT grown with mucin beads than without
179 it. The dynamics of galactose in RI monoculture indicates that RI also hydrolyzed mucin and
180 further utilized its degradation products such as galactose. To investigate the effects of
181 mucin degradation products on the growth of BT and RI at different glucose levels,
182 monosaccharides including Neu5Ac, *N*-acetylgalactosamine, *N*-acetylglucosamine, fucose,
183 galactose, mannose, and their mixture were added to the standard WC medium and WC
184 medium without glucose and pyruvate in 24-well plates. In the presence of
185 glucose/pyruvate, none of the supplemented sugars influenced BT growth significantly ($P >$
186 0.05 by Student's t test) compared to the WC control (Figure S7a). In contrast, Neu5Ac
187 impacted RI growth positively while other sugars had negative effects (Figure S7c). In the
188 absence of glucose/pyruvate, all sugars except Neu5Ac had positive effects on BT growth
189 (Figure S7b), and all sugars, in particular galactose, promoted RI growth (Figure S7d). In
190 conclusion, mucin-derived monosaccharides have species-specific effects that in addition
191 depend on the level of glucose.
192
193 The RNA-seq data further elucidated the different responses of BT and RI to mucin. For BT,
194 we first collected a list of genes/operons associated with the polysaccharide utilization loci
195 of mucin *O*-glycans, which were possibly activated by two types of transcriptional
196 regulators, namely extracytoplasmic function sigma/anti-sigma pair (ECF-σ) and hybrid two-

197 component system (HTCS)[35]. Interestingly, those genes linked to HTCS and ECF-*σ* showed
198 significantly high expression in the lag phase of 4 h (Figure 3a; $P < 0.001$ for both by
199 Student's t test), and genes of ECF-*σ*-linked loci were also expressed after the
200 glucose/pyruvate depletion (48 h and 120 h), indicating BT utilization of mucin *O*-glycan
201 components, which further supports the hypothesis that nutrients derived from mucin were
202 responsible for the long-term survival of BT. Specifically, after glucose/pyruvate ran out at
203 24 h, we observed a significantly ($P < 0.001$ in all cases; Student's t test) increased
204 expression of genes encoding the extracellular galactosidase (BT_3340, 4684) and
205 fucosidase (BT_1842), as well as genes involved in the utilization of galactose (BT_0370-71,
206 0623) and fucose (BT_3606, 1273-75). These results are consistent with BT metabolism of
207 mucin *O*-glycans including galactose and fucose (Figures 2d and S7b). Based on expression
208 levels measured in transcripts per million, RI consistently increased the expression of genes
209 involved in glycolysis, pyruvate utilization, mucin hydrolysis, galactose and mannose
210 utilization, and the butyrate-producing process after depletion of glucose/pyruvate, with or
211 without mucin beads present in the medium (Figures 3b and S3b). At a high
212 glucose/pyruvate level (Figure S8a), the presence of mucin significantly reduced the
213 expression of genes associated with the transport of glucose (RIL182_03793, 03794, 03796),
214 pyruvate (RIL182_01689), galactose (RIL182_01067-69) and *N*-acetylglucosamine
215 (RIL182_02688-89) across the outer membrane. At a low glucose/pyruvate level, our results
216 suggest that mucin impaired the utilization of lactate and acetate. For example, genes of
217 lactate dehydrogenase (RIL182_00335) and butyryl-CoA:acetate CoA-transferase
218 (RIL182_00413) were significantly down-regulated (Figure S8b). Thus, mucin supports the
219 long-term survival of BT, while it undermines RI's growth on glucose/pyruvate and
220 lactate/acetate.
221
222 **Impact of mucin on interaction dynamics**
223 For the co-culture grown in WC, the co-utilization of glucose and pyruvate resulted in two
224 separate density peaks of 7.4 and 4.6×10^5 viable cells/µl for BT and RI, respectively (Figure
225 2c). The pH decreased from 6.7 to 5.3, which was not as acidic as in the BT monoculture
226 (5.0) but lower than in RI monoculture (5.7). After depletion of glucose and pyruvate, BT's
227 viable cell numbers gradually went down, as in monoculture. Interestingly, RI presented a
228 second peak of 4.1×10^5 viable cells/µl at 38 h. In addition, the net concentration of lactate

229 in co-culture was significantly lower than in each monoculture ($P < 0.001$ in both cases;
230 Student's t test). For the co-culture grown in the presence of mucin beads, BT reached a
231 maximal density of 1.5×10^6 viable cells/µl at 16 h, which was two-fold higher than that in
232 WC. RI in the mucin co-culture exhibited significantly lower cell densities than in WC co-
233 culture ($P < 0.01$ by Student's t test), accompanied by a lower maximal density of 1.8×10^5
234 viable cells/µl. The pH of 5.1 was nearly as acidic as in the BT monoculture with or without
235 mucin. A second peak of RI density in mucin co-culture was observed at 120 h,
236 corresponding to a roughly ten-fold increase in density from 96 h to 120 h (Figure S6; mean
237 values of three independent experiments with three biological replicates). The significant (P
238 < 0.001 by Student's t test) increase of galactose in the co-culture compared to the BT
239 monoculture suggests that both species hydrolyzed mucin (Figure 2f).
240
241 To investigate the interaction dynamics of BT and RI and mucin's impact on it, we compared
242 viable cell counts in co-culture and monoculture over time. We computed the interaction
243 strength, here defined as the impact of one organism on the other's abundance, as the log
244 ratio of viable cell counts in liquid in co- versus monocultures. As shown in Figure S9, the
245 interaction strength and in some cases its sign (i.e., positive or negative impact) changed
246 over time for both organisms with and without mucin beads. In the presence of
247 glucose/pyruvate, the competition for these nutrients resulted in negative interaction
248 strengths for both organisms. After depletion of glucose/pyruvate and in the absence of
249 mucin, RI impacts BT positively, likely by increasing the pH in the co-culture compared to the
250 BT monoculture. In the presence of mucin, BT's impact on RI during the initial growth on
251 glucose/pyruvate (20-48 h) changed from negative to positive, likely by reducing the
252 concentration of mucin degradation products that affect RI's growth negatively in the
253 presence of glucose. In summary, changing conditions alter interaction mechanisms
254 between the two species, which lead to varying interaction signs and strengths.
255
256 To further elucidate their changing interaction mechanisms across growth phases, we
257 compared the differential gene expression between co-culture and monoculture (Figure 3c-
258 d). In the presence of RI, BT genes associated with the transport of glucose (BT_0371, 1758)
259 were significantly down-regulated in WC without mucin (Figure 3c; I, II). In addition, the
260 expression of six out of ten glycolysis genes as well as genes involved in succinate, acetate

261 and formate production was significantly lowered in WC at low glucose/pyruvate levels
262 (Figure 3c; II). With mucin, BT up-regulated glycolysis genes and genes involved in producing
263 formate, acetate, succinate and lactate (Figure 3c; III, IV). At low nutrient levels, it also up-
264 regulated genes encoding the exocellular galactosidase (BT_3340, 4684), fucosidase
265 (BT_1842), mannosidase (BT_0458) and sialidase (BT_0455) in response to mucin hydrolysis,
266 and genes associated with the utilization of galactose and *N*-Acetylgalactosamine (Figure 3c;
267 IV). BT genes (BT_0617-22) belonging to the membrane-associated, proton-translocating
268 ferredoxin:NAD^+ oxidoreductase (*Rnf* complex) were also more expressed with mucin
269 (Figure 3c; III, IV). In conclusion, BT down-regulates the genes of glycolysis and pyruvate
270 oxidation when RI is present in WC, but does the opposite in WC and mucin.
271
272 In the presence of BT, RI genes associated with glucose transport (RIL182_03793-94, 03796,
273 01587-88) and the ATP generation via proton pump (RIL182_00203-10) were down-
274 regulated at high and low glucose/pyruvate levels, respectively (Figure 3d; I and II,
275 respectively). A candidate gene of the alarmone ppGpp biosynthesis was significantly up-
276 regulated (RIL182_00174). It is part of RI's response to stress such as carbon starvation and
277 may be involved in triggering its diauxic shift. RI genes associated with the import of glucose
278 (RIL182_03794, 03796), pyruvate (RIL182_01689), galactose (RIL182_01067-69) and *N*-
279 acetylglucosamine (RIL182_02688-89), as well as seven out of ten glycolysis genes were
280 systematically down-regulated at high glucose/pyruvate levels with mucin (Figure 3d; III). In
281 addition, RI genes associated with the butyrate-producing process via butyryl-CoA:acetate
282 CoA-transferase pathway were more expressed when glucose/pyruvate was depleted, with
283 or without mucin (Figure 3d; II, IV). BT restricts RI's import of glucose and assists its
284 production of butyrate from lactate/acetate, regardless of mucin supplementation.

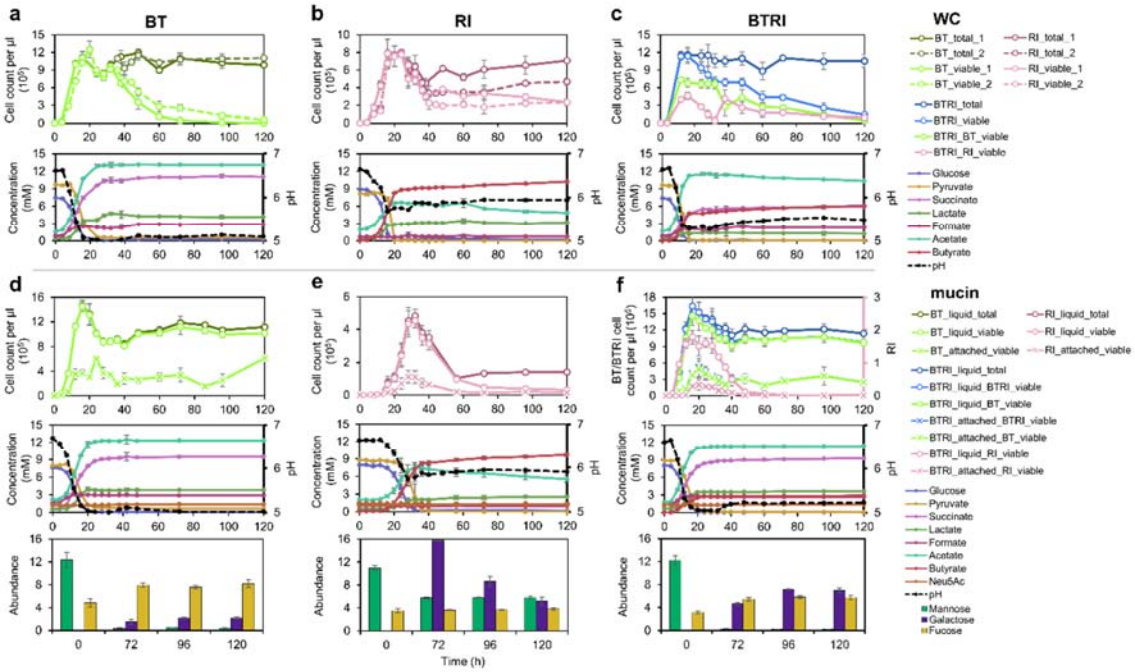

Figure 2. Performance of BT and RI in monoculture and co-culture without and with mucin beads during batch fermentation. Cell density, concentrations of glucose, pyruvate and fermentation products, and pH values for BT monoculture **(a)**, RI monoculture **(b)** and their co-culture **(c)** in WC medium during 120 h cultivation; Cell density, concentrations of glucose, pyruvate and fermentation products, pH values as well as concentrations of mucin monomeric sugars for BT monoculture **(d)**, RI monoculture **(e)** and their co-culture **(f)** in WC with mucin beads during 120 h cultivation. Circles represent the mean values of biological replicates. Error bars indicate the standard deviation of biological replicates (n=3 for BT and RI monocultures in WC experiment 1; n=2 for BT and RI monocultures in WC experiment 2; n=6 for co-culture in WC; n=3 and n=5 for BT and RI monocultures in WC with mucin beads, respectively; n=5 for co-culture in WC with mucin beads). Concentrations of mucin sugars are represented by the integrated area under the peak corresponding to the metabolite. To show the same range on the y axis of barplots, we divided these values by factors of 1,000,000, 5,000,000 and 10,000 for galactose, mannose and fucose, respectively. WC: Wilkins Chalgren medium; BT: *Bacteroides thetaiotaomicron;* RI: *Roseburia intestinalis*; Neu5Ac: *N*-Acetylneuraminic acid.

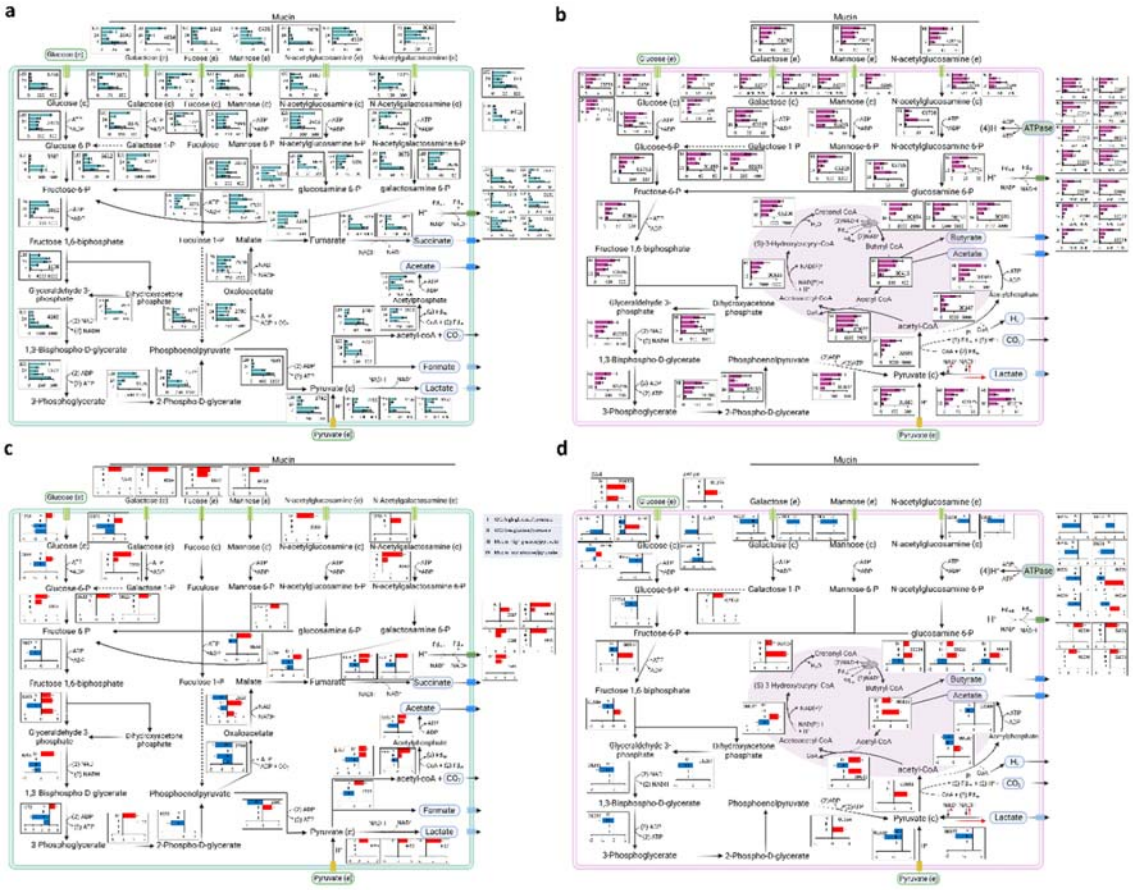

Figure 3. Metabolic maps summarizing gene expression in monocultures and significantly differential expression in co- versus monocultures of BT and RI. Gene expression of the key metabolic routes of glucose and pyruvate fermentation, as well as mucin hydrolysis and mucin sugars utilization in BT **(a)** and RI **(b)** monocultures in WC medium with mucin beads (Supplementary files 3 and 4); differential gene expression between co-culture and monocultures of BT **(c)** and RI **(d)**. In each barplot of **a** and **b**, gene expression levels (x axis) were measured in transcripts per million of RNA samples at time (y axis) 4 h, 12 h, 24 h, 48 h and 120 h for BT, and at time 16 h, 28 h, 40 h and 48 h for RI. In each barplot of **c** and **d**, differential gene expression was calculated with DESeq2 for four categories: high levels of glucose/pyruvate in WC (I), low levels of glucose/pyruvate in WC (II), high levels of glucose/pyruvate in WC with mucin beads (III) and low levels of glucose/pyruvate in WC with mucin beads (IV); positive and negative values of $\log_2$fold-change are shown in red and blue on the x axis, respectively. Numbers in each barplot stand for the Gene ID in the genomes of BT and RI. The solid and dashed lines represent single- and multi-enzyme

319 reactions between the two indicated molecules, respectively. Error bars indicate the
320 standard deviation of three biological replicates. Metabolic maps with gene expression in BT
321 and RI monocultures in WC are shown in Figure S3 and the Supplementary files 3 and 4. ECF:
322 extracytoplasmic function sigma/anti-sigma pair; HTCS: hybrid two-component system;
323 GlcR: HTH-type transcriptional repressor of glucose; ppGpp: alarmone guanosine-5'-3'-
324 bispyrophosphate.
325
326 **Kinetic model reproduces the observed dynamics**
327 To reproduce physiological observables such as total and viable cell counts as well as
328 concentrations of key nutrients and metabolites, we developed a model with ordinary
329 differential equations that summarizes our understanding of the interaction mechanisms
330 (Figure 4a). Since we see a roughly linear relationship between counts of viable attached
331 and free-swimming cells (Figure S10), the model assumes that a fixed fraction of the cells
332 attaches to mucin beads and that only these cells can degrade mucin. Mucin is treated as an
333 inexhaustible resource. We further assume that changes in SCFAs fully determine changes in
334 the pH, since we observed a strong linear relationship between pH and the sum of the
335 concentrations of SCFAs (Figure S11). Based on the literature, we also assume that a low pH
336 affects the growth of BT more strongly than that of RI, i.e., BT is more sensitive to acidity[36].
337 In addition, BT and RI can both grow on glucose and mucin sugars, which was well-
338 supported by our fermentation data and also confirmed at the transcriptional level. Given
339 our microtiter plate data, we further assume that mucin degradation products inhibit RI's
340 growth on glucose (Figure S7c). RI only switches to its lactate/acetate-consuming slow
341 growth mode when the concentrations of glucose and mucin degradation products are low
342 (Figure S8b). Finally, we hypothesize that glucose inhibits BT's growth on mucin sugars,
343 which is supported by the significant overexpression of the cAMP-Crp gene in the presence
344 of glucose ($\log_2$fold-change of BT_2187 in mucin monoculture: 1.7 for 4 h vs 12 h, 3.6 for 4 h
345 vs 24 h and 1.8 for 12 h vs 24 h). We simplified the model by treating glucose and pyruvate,
346 acetate and lactate as well as mucin sugars as single entities (see model scheme in Figure
347 4a). The slow growth mode of RI and the behavior of BT on mucin after depletion of sugar
348 are represented by separate states (in both cases referred to as 'slow growth mode').
349 Parameter values including metabolite production and consumption as well as state

switching rates were determined manually. The equations, parameter values and initial conditions are given in the Supplementary file 2.

The model qualitatively reproduces our observations, including the second peak observed for BT at 32 h in WC monoculture, the long-term survival of RI in WC and of BT in the presence of mucin beads (Figure 4b). However, the model fails to reproduce the second peak for RI in WC in co-culture, implying that additional mechanisms are at play that are not yet fully understood.

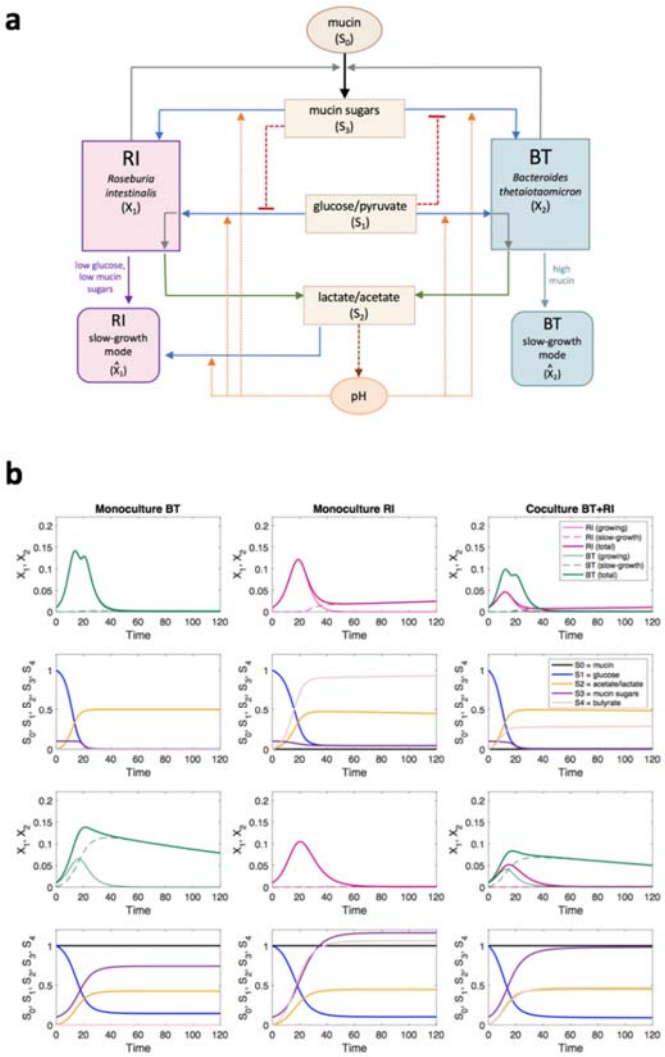

Figure 4. Model scheme and simulations reproducing observations qualitatively. a, Scheme of the kinetic model. **b**, Dynamics generated by the model without and with mucin. The equations, parameter values and initial conditions are given in Supplementary file 2.

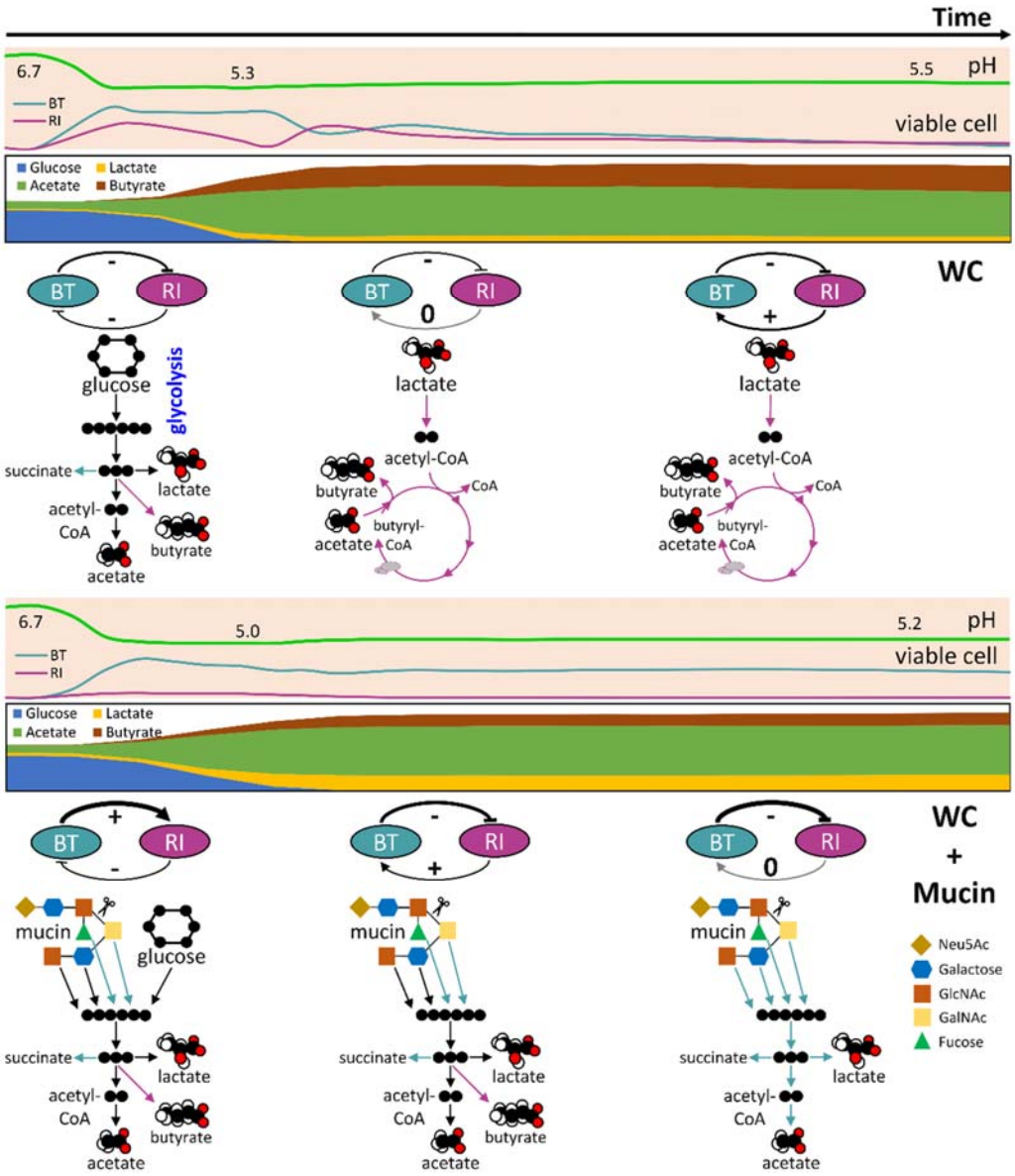

Figure 5. Summary of the interaction mechanisms driving abundances and metabolite concentrations in the BT and RI co-cultures without and with mucin beads. Signs of positive, negative and absence of an interaction are shown as +, - and 0, respectively. The thickness of the arrow represents the interaction strength quantified as the logarithm of viable cell density ratios in co- versus monocultures (detailed in Figures S9 and S12). Main metabolic pathways including glycolysis, converting lactate/acetate to butyrate, mucin hydrolysis and mucin sugars utilization are colored in teal, pink and black for BT, RI and both, respectively. Neu5Ac: *N*-acetylneuraminic acid**;** GlcNAc**:** *N*-acetylglucosamine; GalNAc: *N*-acetylgalactosamine.

374 **Discussion**

375 Here, we systematically investigated the molecular mechanisms underlying the ecological
376 interactions between two representative gut bacteria in the presence of simple and
377 complex carbon sources within a spatially structured environment (Figure 5). Our results are
378 in agreement with known niches in the human gut: BT survives as a mucus resident and RI
379 prefers to stay in the lumen[17,32].
380
381 We found that even when feeding on similar resources, BT and RI used alternative strategies
382 to cope with and anticipate nutrient scarcity. Growth data combined with temporal gene
383 expression patterns suggest that BT acts as a 'funnel' with its central carbon/energy
384 metabolism capable of tapping several monosaccharides. Independent entry points are
385 funneled into glycolysis until phosphoenolpyruvate is produced, which is converted into
386 oxaloacetate by fixing a CO_2 molecule with the generation of an extra ATP[37]. CO_2 could be
387 supplied from either the external environment or the conversion of pyruvate to acetyl-CoA.
388 Although this strategy results in accelerated growth, it comes at the cost of significantly
389 inferior performance when actively consumed nutrients are depleted. In contrast, RI uses
390 carbon chain elongation to generate additional energy and maintain a redox balance (Figure
391 3b), resulting in butyrate production. Although its growth is slower than that of BT, it can
392 switch its energy source to acetate and lactate, which are also produced by BT. This diauxic
393 shift resembles the nutrient utilization strategies adopted by other bacterial species[38],
394 mostly well characterized in *E. coli* [39–42]. Some butyrate producers such as RI can overcome
395 the energetic barrier to convert lactate to pyruvate by employing the flavin-based electron
396 confurcation: driving electron flow from lactate to NAD^+ at the cost of exergonic electron
397 flow from reduced ferredoxin to NAD^+. However, producing butyrate from lactate and
398 acetate is a much lower energy-yielding process, compared to glucose[34]. Slow growth is also
399 a known strategy to deal with starvation in other nonsporulating bacteria[43].
400
401 BT's growth strategy results in a dramatic reduction in the environmental pH, which
402 significantly inhibits its own growth. This self-inhibition resembles the hypothesis of
403 ecological suicide suggested by Ratzke et al. with some additional complexity[44]. At low pH,
404 BT cells remain viable for an extended period of time when mucin beads are present.

405 Without mucin, when glucose and pyruvate are depleted, a loss of viability is observed
406 throughout the population (Figure 2a). The depletion of nutrients per se is probably not the
407 cause of this loss since when the pH was restored in a spent medium assay, the BT cells
408 metabolized an alternative carbon source and restored growth (Figure S1). Taken together,
409 these results suggest that similar to other bacteria[45], BT requires an energy source to be
410 metabolically active in an acidic environment, possibly channeling its ATP from growth to
411 maintaining its intracellular pH within a physiologically viable range. When this source of
412 energy is no longer available, cells quickly lose viability and no longer have the opportunity
413 to utilize new nutrients. Interestingly, pH also opens up a new dimension in the ecological
414 interactions between BT and RI, particularly in WC medium. As shown in Figure 5, although
415 the two species compete for glucose and pyruvate, and thus initially sustain a negative
416 interaction, the glucose and pyruvate that RI manages to consume result in a smaller
417 decrease in the environmental pH (since RI does not lower the pH as much as BT), leading to
418 an indirect positive effect on BT at later stages.
419
420 We highlighted the asymmetries in the way BT and RI respond to mucin, whose positive or
421 negative effect depends on the presence or absence of glucose during fermentation. In the
422 absence of glucose, most of the mucin sugars tested boost BT's growth, except for Neu5Ac.
423 Analysis of its genome reveals the absence of a Neu5Ac lyase (*nanL*) gene. BT is unable to
424 catabolize Neu5Ac and did not grow on it in a minimal medium[46,47]. As mucin beads and the
425 tested mucin sugars did not significantly affect BT's growth during glucose fermentation
426 (Figure S7a), we assume that glucose prevents BT from simultaneously consuming other
427 carbon sources. This assumption was also necessary to reproduce BT's behavior with our
428 model. In *E. coli*, further uptake of carbon sources is suppressed by the transcriptional
429 regulator cAMP-Crp when nutrient uptake surpasses anabolism[38]. Here, we found that a
430 candidate gene of cAMP-Crp (BT_2187) was significantly over-expressed when BT consumed
431 glucose. As BT was reported to easily switch its metabolism from dietary input to mucin
432 glycans[17], we assume that BT relies on cAMP-Crp regulation to cope with excessive carbon
433 flux. In contrast to BT, RI does not grow well when glucose and mucin are supplied together
434 (Figure 2e). Adding mucin beads also significantly up-regulated the gene of HTH-type
435 transcriptional repressor GlcR (RIL182_03930), which indicated the repression of glucose
436 catabolism by RI. As no cAMP-Crp genes were found in its genome, we assume that glucose

437 and mucin sugars may compete for ATP-binding cassette transporters. Combined with
438 slower growth on mucin sugars, this may explain the negative effects of mucin sugars on RI's
439 growth on glucose. This is also supported by its significantly increased abundance in the
440 mucin co-culture (Figure 5), which likely resulted from a decreased concentration of mucin
441 sugars such as mannose due to uptake by BT. However, a mechanism of RI's carbon uptake
442 strategy has to be explored further.
443
444 Glycan-mediated attachment was reported as an important strategy for gut bacteria to
445 access nutrients[8]. Since both BT and RI attached to the mucin beads, the physical proximity
446 could influence their interactions on the beads. The beads were also not saturated by cells,
447 illustrated by a roughly linear relationship between density on beads and in the liquid of co-
448 culture (Figure S13). In addition, the observed fast attachment and detachment implies that
449 the dynamics between attached and free-swimming cells may be tightly coupled. Spatial
450 transcriptomics at a single-cell resolution may further reveal the interaction mechanisms of
451 human gut bacteria in a spatial context[48].
452
453 In the presence of BT, RI exhibited additional density peaks at 38 h without mucin and at
454 120 h with mucin, which were not predicted by our model. In most of the cases, the
455 classification technique we used showed high accuracy in distinguishing BT and RI on a basis
456 of their optical characteristics in flow cytometry, and the method accuracy was confirmed
457 with the data of a GFP labelled BT (Figure S14). However, when the cells are losing viability
458 (Figure 2c, 24-38 h), the similarity between live and inviable cells causes difficulties in
459 species separation. Thus, the transition from the first peak of viable RI cells to the second in
460 the WC co-culture may be smoother than observed. There are also alternative explanations
461 for the peak. Since BT can produce a higher concentration of lactate than RI in monoculture,
462 a transiently sufficient amount of lactate in the presence of BT may reverse the flow from
463 lactate to pyruvate in RI so that lactate is consumed instead of produced. In addition, under
464 the stress of an acidic pH BT may release toxins that contribute to the loss of viability of RI[49].
465 Some viable cells of RI may also grow by necrophagy on accumulated dead cells[50].
466
467 We found that interaction strength significantly varies in value and sign along the growth
468 curve, both with and without mucin (Figure 5), due to the variability in pH and nutrient

levels. Widely used population models such as the generalized Lotka-Volterra assume interaction strengths to be constant. This is problematic, because even if environmental conditions are controlled, bacteria themselves will frequently alter their environment and hence their interaction mechanisms. Thus, the generalized Lotka-Volterra is only applicable in systems where environmental conditions (including pH and nutrient levels) are kept constant, i.e., chemostats. However, the intestine is not well described by a chemostat, since nutrient levels, moisture and pH fluctuate with the daily intake of meals and the circadian rhythm[51,52]. To cope with this, models can either account for changing interaction strengths as done here, which requires knowledge of interaction mechanisms and parameter values, or average over interaction strengths encountered in typical scenarios in the environment of interest. Such an ensemble approach may better represent the interaction between two organisms than the usual 'snapshot' strategy of quantifying interactions in one particular condition but may not lend itself to predictive modelling. Thus, changing interaction strengths are a challenge for predictive models of human gut microbiota.

A deeper understanding of alternative metabolic strategies and changing species interactions in gut microbiota is necessary to rationally design next-generation probiotics and to predict the outcome of fecal microbiota transplantation. By deciphering the interaction mechanisms between two common gut bacteria across changing conditions, we have taken another step towards this goal.

490 ## Methods

491 **Human gut bacterial strains**

492 Bacterial strains of *Bacteroides thetaiotaomicron* VPI-5482 (DSM 2079^T) and *Roseburia*
493 *intestinalis L1-82* (DSM 14610^T) were obtained from the Deutsche Sammlung von
494 Mikroorganismen und Zellkulturen (DSMZ, Germany). The strains were frozen in Wilkins-
495 Chalgren Anaerobe Broth (WC; Oxoid Ltd., Basingstoke, United Kingdom) plus 20% glycerol
496 and maintained at -80°C until use.

497

498 **Mucin bead preparation**

499 Mucin beads were generated based on a protocol previously described[53]. Briefly, a
500 polysaccharide gel was prepared that contained (in g/100ml) Gelrite gellan gum (2.5, Sigma),
501 xanthan gum (0.25, Sigma) and porcine mucin type II (5, Sigma). The dried powders were
502 suspended in 100 ml of 90°C pre-heated distilled water containing 0.2 g sodium citrate
503 (Sigma) and 350 µl 10 M NaOH. This polymer solution was mixed until dissolved and then
504 autoclaved for 20 min at 121°C. The bead generation was performed under sterile
505 conditions and was based on a two-phase dispersion process[54]. The autoclaved solution was
506 cooled down to 50°C on a heater and slowly poured with a distance of 40 cm into 45°C
507 sunflower oil while keeping the stirring speed at 300 rpm, to obtain a suspension of aqueous
508 gel droplets in the hydrophobic phase. Gel beads were formed when cooling the suspension
509 down to 15°C on ice. The oil was carefully washed off the beads and were subsequently
510 hardened by soaking in a 0.1 M $CaCl_2$ solution (adjusted to pH 5.2) for 20 min at room
511 temperature. Beads with a diameter of 500 µm were selected by wet sieving and stored at
512 4°C in aseptic conditions until use.

513

514 **Cultivation and sample collection**

515 Serum bottles (120 ml) containing 60 ml WC medium and around 8000 mucin beads were
516 used as a spatially structured system to grow BT and RI. Briefly, each bottle was first filled
517 up with 50 ml WC medium, and 3 g wet mass of 500 µm mucin beads in 10 ml WC were
518 pipetted into each bottle under sterile conditions. The bottles were transferred to the
519 anaerobic workstation (Don Whitley A35 with HEPA filter; 10% H_2, 10% CO_2, 80% N_2, 55%
520 humidity) to be deoxygenated for 120 h. Oxygen-free conditions in liquid and in the beads

521 were confirmed through the color change of redox indicator resazurin. The bottles were
522 closed with rubber stoppers and sealed with aluminum caps that were UV sterilized for 1 h
523 in a laminar flow chamber before use. For bottle experiments without mucin beads, bottles
524 were filled with 60 ml WC medium that was prepared in the same way as described above.
525
526 To prepare the inoculum, 100 µl of BT or RI from frozen stocks was first inoculated in a 10-
527 ml Wheaton® serum vial containing 5 ml WC medium as preculture. These serum vials were
528 prepared by adding autoclaved medium and were deoxygenated in the anaerobic
529 workstation for 24 h. The vials were closed with rubber stoppers and sealed with aluminum
530 caps before use. After 16 h, each species' preculture was diluted to an OD_{600} of 0.1
531 determined by a portable spectrometer (DR1900; Hach Lange GmbH, Germany) and used as
532 the inoculum. The serum bottles were inoculated with 1 ml of the diluted preculture and
533 were incubated at a constant stirring rate of 170 rpm at 37°C in a shaker (KS 4000 i; IKA,
534 Staufen, Germany). Cultivations of the monoculture and co-culture were followed for 120 h
535 after inoculation, with samples taken from both the liquid and beads every four hours for
536 the first 48 h and every 12 h afterwards. For further investigation of the BT and RI growth
537 and their interactions in the long term, an experiment was designed for the co-culture to
538 follow for 288 h with samples taken every 24 h since 120 h after inoculation. All experiments
539 were performed at least in three biological replicates and always had a negative control
540 bottle without inoculation but with sampling for each time, to verify its sterility.
541
542 For each time point, two milliliters of the fermentation broth containing the suspended
543 mucin beads were sampled to 2-ml Eppendorf tubes. The serum bottles were opened and
544 closed carefully each time to avoid contamination in the anaerobic workstation. During
545 sampling the beads settled downward to the bottom within seconds. The supernatant was
546 carefully pipetted into new 2-ml tubes in the anaerobic workstation, and subsequently was
547 used to measure pH (PH-922, ISFET, Japan) and OD_{600}, and to profile metabolites as well as
548 quantify bacterial cell counts by live/dead staining followed by flow cytometry.
549
550 **Spent media and pH preference experiments**
551 Several spent media assays were conducted in serum bottles to clarify how BT and RI
552 interact with each other, and how abiotic factors influenced their growth. First, we grew a

553 culture of BT in WC for 48 h without mucin beads and sterilized the spent medium through a
554 filtration with 0.2-µm sterile syringe filters (PES; VWR International). In addition, the filtered
555 medium was autoclaved and deoxygenated for 24 h in the anaerobic workstation. Four
556 conditions were prepared to cultivate BT in the spent medium: *i*) the original spent medium
557 without adjusting pH (pH 5) and without adding carbon source, *ii*) spent medium with pH
558 adjusted to 6.5, *iii*) spent medium with glucose and pyruvate added in the same
559 concentrations as in WC at pH 5 and *iv*) spent medium with added glucose and pyruvate
560 plus pH adjusted to 6.5. We grew BT in three biological replicates in the serum bottles for a
561 period of 48 h and sampled every 8 h for measuring pH, OD_{600}, metabolites and live/dead
562 cell counts. Second, we grew BT in WC plus mucin beads in different periods of 24 h, 48 h
563 and 72 h, as well as in WC without mucin beads for 48 h. The cell- and oxygen-free spent
564 media were prepared in the same way as described above, and the pH was adjusted to 6.5
565 before autoclaving.
566
567 We further adjusted the pH of WC medium to the specified values of 4.5, 5.0, 5.5 and 6.0 by
568 using 1 M HCl solution, and also included the original WC of pH 6.7 for testing in serum
569 bottles. The growth of BT was followed for 48 h, with samples taken at 0 h, 4 h, 8 h, 12 h, 24
570 h, 36 h and 48 h and measured as described above.
571
572 **Detachment experiment**
573 To estimate the rate at which bacterial cells detach from particles, we followed the
574 population change of planktonic cells in a fresh WC medium, into which mucin beads with
575 attached BT cells were added. We first grew BT culture in a serum bottle containing 60 ml
576 WC plus mucin beads, with a same inoculum size as described: 1 ml of OD_{600} 0.1. After 24 h
577 cultivation, 2 ml of the fermentation broth containing the suspended mucin beads were
578 sampled to each 2-ml tube. 0.5 ml of phosphate buffer (PBS, pH 7.3; Invitrogen, Thermo
579 Fisher Scientific, USA) was added to each tube after washing with 1 ml PBS. The beads in PBS
580 were transferred to a 12-well plate (Sarstedt, Germany), with 1.5 ml sterile WC medium in
581 each well. For comparison, we included wells of fresh WC medium and WC medium
582 supplemented with sterile mucin beads, both of which were inoculated with BT in a volume
583 of 25 µl of OD_{600} 0.1. The experiment was performed in four replicate wells for each group.
584 The plates were incubated at a constant stirring rate of 170 rpm at 37°C, with liquid samples

585 taken at 0 min, 30 min, 60 min, 90 min, 150 min and 240 min for live/dead cell staining
586 followed by flow cytometry.
587
588 **Mucin monomeric sugar assays**
589 The degradation products of mucin including Neu5Ac, *N*-acetylgalactosamine, *N*-
590 acetylglucosamine, fucose, mannose and galactose were tested for their effects on the
591 growth of BT and RI. The tests for each species were performed by using 24-well plates
592 (Sarstedt, Germany) filled with two types of media: the standard WC and WC without
593 carbon sources glucose and pyruvate. Each medium was split into eight aliquots, each of
594 which was supplemented with either one of those mucin sugars in 1 mM or a mixture of all
595 six sugars together in 1 mM or without any sugar added as the control. We first inoculated
596 0.5 ml preculture with OD_{600} 0.1 to 20 ml of each aliquot, and then transferred 1.2 ml to
597 each well in three replicates. The plates of BT or RI were incubated at a constant stirring rate
598 of 120 rpm at 37°C for 24 h or 48 h, respectively, with samples taken every 12 h for pH and
599 live/dead staining followed by flow cytometry measurements.
600
601 **Quantification of bacterial cell counts using flow cytometry**
602 DNA-based staining using SYBR Green I (SG; Invitrogen) in combination with propidium
603 iodide (PI; Invitrogen) was applied to quantify and differentiate bacterial cells with intact
604 and damaged cytoplasmic membranes following the protocols described before[55]. Briefly,
605 the stock staining solution contained per ml: 10 µl of SG (10,000 concentrate), 20 µl of 20
606 mM PI and 970 µl of the filtered dimethylsulfoxide. Cells of the fresh culture in liquid from
607 different time points were diluted in a filter-sterilized PBS buffer for the live/dead cell
608 staining. Dilutions in 1:10 and 1:200 were performed for the first two time points (0 h and 4
609 h) and the later time points (after 8 h), respectively. Under anoxic conditions, cell samples
610 were diluted in 1-ml 96-well plates (Eppendorf, Germany) and stained with 3 µl of the SG/PI
611 staining solution, and subsequently were incubated for 20 min in the dark at 37°C right
612 before flow cytometric measurements. To quantify the attached cell counts, the mucin
613 beads sampled from different time points were first washed with 1 ml filter-sterilized PBS in
614 2-ml Eppendorf tubes. After carefully removing the supernatant, we added another 0.5 ml
615 PBS to the tubes that later were sonicated in the water bath of an ultrasonic cleaner
616 (USC200TH, VWR International) for 5 min at 45 kHz. The fresh detached cells in PBS were

617 diluted 1:10 in 96-well plates for all time points and were used for the live/dead cell staining
618 as described above. To confirm method accuracy, we also used a green fluorescent protein
619 (GFP)-tagged BT containing the modified plasmid pWW3452 (CTAATG in the start codon of
620 GFP was replaced with CATATG), which can stably fluoresce when grown anaerobically with
621 subsequent exposure to oxygen for 60 min as described[56].
622
623 Flow cytometric counts of the fresh cells were obtained by using a benchtop CytoFLEX S flow
624 cytometer (Beckman Coulter, Brea, USA), equipped with the identical lasers and detectors
625 as described previously[57]. Cell events of each sample were recorded for 1 min at a sample
626 flow rate of 10 µl/min, using the CytExpert software (version 2.4.0.28). Threshold values of
627 3,000 and 2,000 were applied to the channels of forward scatter and side scatter,
628 respectively. These thresholds were selected based on our tests of BT and RI cells from
629 different growth phases in serum bottles containing WC medium without and with mucin
630 beads to exclude most of the background events and to obtain accurate cell counts. In
631 addition to the instrumental calibration with CytoFLEX Daily QC Fluorospheres, 0.5 µm and 1
632 µm green fluorescent beads (Thermo Fisher Scientific, USA) were applied to each batch of
633 experiments as internal standards, to monitor the instrument stability and to make
634 cytometric data from different batches more comparable.
635
636 **Flow cytometry data processing**
637 We quantified the absolute abundance of BT and RI cells by clustering populations of flow
638 cytometric events in a UMAP[58] space using an in-house developed pipeline. The detailed
639 protocol and scripts necessary to reproduce our cell population counts are available in:
640 bit.ly/3WNrslL. Briefly, raw flow cytometry data from all channels were normalized and
641 scaled. Since flow cytometry data values have approximately log-normal distributions and
642 contain negative values, we first transformed the data with the arcsinh function and then
643 scaled it to exhibit uncorrelated unit variances and means around zero. Next, we projected
644 the transformed data into a three-dimensional UMAP space using the Euclidean distance as
645 a metric, and parameters of 25 and 0.1, respectively, for the number of neighbors and
646 minimum distance. Using flow cytometry runs containing cells and runs containing only the
647 media (blank) we first classified the events into four categories: (1) “live” (events in the
648 UMAP space that are SG positive, PI negative, and not in the blanks); (2) “inviable” (events

649 that are not in the blanks, but PI positive) and; (3) “debris” (events that are PI and SG
650 negative, but not in the blank files); (4) “blank” (events that overlap with the blank files). PI
651 and SG positive events were determined based on a threshold signal in their respective
652 channels, which were empirically estimated from the distribution of all the data samples.
653 The overlap with blank events from blank control files was determined by drawing a circle
654 around the points in the blank files, whose radius is proportional to the density of blank
655 points found in its proximity and classifying the area spanned by this circle as blanks in a
656 combined UMAP projection of samples and blank files. Only the events classified as ‘live’
657 were selected for the next steps. We then used the monoculture samples of each respective
658 time point to classify cells in the co-culture samples. For this we first built a training space
659 consisting of a labeled UMAP projection of 5,000 random events selected from each
660 monoculture biological replicate. Next, we used supervised UMAP to reproject the
661 monoculture and co-culture live-cell events into the training space. We then used the *K*-
662 nearest neighbors vote classifier (with parameters: n_neighbors = 50, weights = distance,
663 and metric = Mahalanobis) to identify the species labels of the co-culture events based on
664 their proximity to the monoculture events in the supervised UMAP space.
665
666 **Contamination check and confirmation of abundance profiles with 16S**
667 Sanger sequencing of 16S rRNA genes was performed regularly to check each strain identity.
668 In addition, we selected four biological replicates for each time point from the co-cultivation
669 experiments of BT and RI in WC with and without mucin beads, to confirm the abundance
670 profile of BT and RI in co-culture with 16S rRNA gene amplicon sequencing (Figure S15).
671 Sequencing of Illumina MiSeq and downstream analysis was performed as described
672 previously[57].
673
674 **Metabolite profiling**
675 Liquid samples in 1 ml were collected and centrifuged for 20 min at 21,130 × *g* at 4°C
676 (Centrifuge 5424 R; Eppendorf, Hamburg, Germany). The supernatants were used for
677 chemical analyses by applying external standards for calibration and quality control. The
678 concentrations of trehalose, glucose, pyruvate, succinate, formate, acetate, lactate, *n*-
679 butyrate and Neu5Ac were determined by high-performance liquid chromatography (HPLC).
680 HPLC analysis was carried out on an Agilent 1200 series HPLC system (Agilent Technologies,

681 USA) equipped with a Bio-Rad Aminex HPX-87H column (Biorad, USA) and a refractive index
682 detector at 40°C. Samples in 20 µl were injected and eluted for 60 min using 5 mM H_2SO_4 as
683 the mobile phase at a flow rate of 0.6 ml/min.
684
685 Concentrations of mucin monomeric sugars galactose, fucose and mannose were relatively
686 quantified by using gas chromatography, carried out by the Metabolomics Core of KU
687 Leuven. The supernatant in 100 µl of each sample was diluted to 1 ml in 80% methanol, and
688 left overnight to allow the precipitation of lipids and proteins. After centrifugation, 100 µl of
689 the supernatant was transferred and evaporated to dryness on a speedvac. A 2%
690 methoxyamine solution was prepared by dissolving methoxyamine hydrochloride (Supelco,
691 ref. 226904-5g) in pyridine (Sigma-Aldrich, ref. 270970-1L). 25 µl of the methoxyamine
692 solution was added to each sample and left to react for 1.5 h at 37°C for methoximation of
693 the hexoses. Afterwards, 80 µl N,O-Bis(trimethylsilyl)trifluoroacetamide with 1%
694 trimethylchlorosilane (Supelco, ref. 15238) was added and left to react for 30 min at 60°C
695 for trimethylsilylation of the methoximated hexoses. One microliter of each methoximated
696 and trimethylsilylated sample was injected by 2:1 split injection by an Agilent Technologies
697 7693 autosampler (Agilent Technologies, Santa Clara; California) into an Agilent 7890A gas
698 chromatograph equipped with a fused silica capillary column (0.25 mm × 30 m) with a
699 chemically bonded 0.25 µm HP-5MS stationary phase (Agilent J&W GC columns, Folsom;
700 California, ref 19091S-433). The injector temperature was 250°C, and the septum purge
701 flowrate was 3 ml/min. The helium flowrate through the column was 0.9 ml/min. The
702 column temperature was held at 160°C for 23.5 min and then increased by 100°C/min to
703 300°C, with 1 min holding there. The column effluent then entered an Agilent 7000 triple
704 quadrupole mass spectrometer. Temperatures of the transfer line and electron impact ion
705 source were 250°C and 230°C, respectively. Ions were generated by a 70 eV electron beam.
706 Spectra were acquired in a selected ion monitoring mode, with fragment masses based on
707 the analyses of standards.
708
709 **RNA extraction and sequencing**
710 We included a total of 69 samples representing the different growth phases of BT and RI in
711 three biological replicates for RNA sequencing, which were selected from the following six
712 independent experiments: monoculture BT in WC (4 h, 12 h and 36 h), monoculture RI in

713 WC (4 h, 12 h and 48 h), coculture BT and RI in WC (12 h , 24 h and 36 h), monoculture BT in
714 WC plus mucin beads (4 h, 12 h, 24 h, 48 h and 120 h), monoculture RI in WC plus mucin
715 beads (16 h, 28 h, 40 h and 48 h), and coculture BT and RI in WC plus mucin beads (6 h, 12 h,
716 24 h, 48 h and 120 h).
717
718 Total RNA was extracted and purified from RNAprotect-treated (Qiagen, Hilden, Germany)
719 frozen liquid samples using the phenol-free RNeasy Plus Mini Kit (Qiagen) according to the
720 instructions of the manufacturer. The cell pellets from -80°C were first lysed by adding the
721 lysis buffer RLT from the kit with 10 µl/ml β-mercaptoethanol. The content of PowerBead
722 tube (glass, 0.1 mm; Qiagen) was further added to the lysate prior to using a bead beater
723 (TissueLyser II, Qiagen) for homogenizing the mixture for 5 min at a speed of 30 beats/sec.
724 Other steps were performed by following the instructions. The eluted RNA samples in
725 nuclease free water were stored at -80°C until use. RNA concentrations were determined
726 with a Nanodrop ND 1000 spectrophotometer (Thermo Fisher Scientific, USA) and a Qubit
727 2.0 fluorometer using the Qubit RNA High Sensitivity Assay Kit (Invitrogen). Samples with a
728 260/230 absorbance ratio below 0.5 were purified using the MinElute PCR Purification kit
729 (Qiagen) and re-measured afterwards, with all samples above 0.5 after purification. RNA
730 integrity and yield were evaluated using RNA Nano and Pico 6000 LapChips (Agilent
731 Technologies, Santa Clara, CA, USA) run on an Agilent 2100 Bioanalyzer (Agilent
732 Technologies).
733
734 Library preparation and sequencing of RNA-seq libraries were carried out by the Genomics
735 Core of KU Leuven. All samples were prepared using the NEBNext Ultra II Directional RNA
736 Library Prep Kit for Illumina (New England BioLabs, #E7760L), with an initial amount of 100
737 ng total RNA in 12 µl. Bacterial rRNA depletion was proceeded using the rRNA Depletion Kit
738 (Bacteria) (New England BioLabs, #E7850L), and the residual mRNA was quality controlled
739 and converted to the libraries that were sequenced on a NovaSeq 6000 (Illumina, San Diego,
740 CA, USA) on a v1.5 S4_300 kit in XP mode. The resulting data of paired-end reads in fastq file
741 format were obtained and demultiplexed before further analysis.
742
743 **RNA-seq data processing**

744 The analysis of the raw sequencing reads was performed as follows: low quality reads and
745 adapters were trimmed with fastp[59]. High quality RNA reads were mapped to their
746 respective reference transcripts with Salmon run in a selective alignment mode and with a
747 decoy-aware index constructed from each organism's genome[60]. The latest reference
748 genomes and transcripts for BT and RI were downloaded from the ensemble bacteria[61] and
749 BV-BRC databases[62], respectively:
750 GCA_000011065.ASM1106v1.dna.toplevel.fa (*B. thetaiotaomicron* VPI-5482),
751 GCA_000011065.ASM1106v1.cds.all.fa (*B. thetaiotaomicron* VPI-5482),
752 GCA_900537995.1_Roseburia_intestinalis_strain_L1-82_genomic.fna (*R. intestinalis* L1-82),
753 GCA_900537995.1_Roseburia_intestinalis_strain_L1-82_cds_from_genomic.fna (*R.*
754 *intestinalis* L1-82). Raw transcript counts were extracted from salmon's output and used for
755 differential gene expression analysis. COG categories, COG numbers and KO numbers were
756 extracted from NCBI COG and KEGG database[63,64], for BT. To obtain annotations for RI, we
757 mapped the respective transcripts to the eggNOG database v5.0 with the eggNOG-mapper
758 2.1.9[65,66].
759
760 **Statistics**
761 To measure gene expression levels, we used methods of transcripts per million and
762 DESeq2's median of ratios to normalize RNA read counts[33]. A strict cutoff of at least 1.5-fold
763 change and a Benjamini-Hochberg adjusted *P* value less than or equal to 0.01 were applied
764 for differential gene expression calculated by DESeq2. Other statistical analyses were
765 performed using R (version 4.2.0).
766
767 **Modelling**
768 Details of model definition and parameterization can be found in the Supplementary file 2.
769
770 **Data availability**
771 Raw amplicon sequencing data and RNA-seq data have been deposited to the Sequence
772 Read Archive database under accession numbers of SAMN32182740-827 and
773 SAMN32321133-55, respectively (https://www.ncbi.nlm.nih.gov/bioproject/PRJNA911421/
774 and https://www.ncbi.nlm.nih.gov/bioproject/PRJNA914119/). Raw flow cytometry data

775 have been deposited to flowrepository.org, under Repository IDs of FR-FCM-Z6YM, FR-FCM-
776 Z6YN, FR-FCM-Z6YP, FR-FCM-Z6YQ, FR-FCM-Z6YR, FR-FCM-Z6YS, FR-FCM-Z6YT, FR-FCM-
777 Z6YU, FR-FCM-Z6YV and FR-FCM-Z6YX, and will be made available upon acceptance of this
778 work. The processed RNA-seq data, flow cytometry data and fermentation data are
779 available at: https://github.com/msysbio.
780

781 **Code availability**

782 Flow cytometry data processing: bit.ly/3WNrslL, MATLAB file for the kinetic model and RNA-
783 seq processing scripts: https://github.com/msysbio.
784

785 **References**

786 1. Donaldson, G. P., Lee, S. M. & Mazmanian, S. K. Gut biogeography of the bacterial
787 microbiota. *Nat. Rev. Microbiol.* **14**, 20–32 (2015).
788 2. Tropini, C., Earle, K. A., Huang, K. C. & Sonnenburg, J. L. The Gut Microbiome:
789 Connecting Spatial Organization to Function. *Cell Host Microbe* **21**, 433–442 (2017).
790 3. Nadell, C. D., Drescher, K. & Foster, K. R. Spatial structure, cooperation and
791 competition in biofilms. *Nat. Rev. Microbiol.* **14**, 589–600 (2016).
792 4. Welch, J. L. M., Hasegawa, Y., McNulty, N. P., Gordon, J. I. & Borisy, G. G. Spatial
793 organization of a model 15-member human gut microbiota established in gnotobiotic
794 mice. *Proc. Natl. Acad. Sci. U. S. A.* **114**, E9105–E9114 (2017).
795 5. Hoek, M. J. A. va. & Merks, R. M. H. Emergence of microbial diversity due to cross-
796 feeding interactions in a spatial model of gut microbial metabolism. *BMC Syst. Biol.*
797 **11**, 56 (2017).
798 6. Lowery, N. V. & Ursell, T. Structured environments fundamentally alter dynamics and
799 stability of ecological communities. *Proc. Natl. Acad. Sci. U. S. A.* **116**, 379–388 (2019).
800 7. Geng, J., Ji, B., Li, G., López-Isunza, F. & Nielsen, J. CODY enables quantitatively
801 spatiotemporal predictions on in vivo gut microbial variability induced by diet
802 intervention. *Proc. Natl. Acad. Sci. U. S. A.* **118**, (2021).
803 8. Patnode, M. L. *et al.* Strain-level functional variation in the human gut microbiota
804 based on bacterial binding to artificial food particles. *Cell Host Microbe* **29**, 664–
805 673.e5 (2021).

806 9. Desai, M. S. *et al.* A Dietary Fiber-Deprived Gut Microbiota Degrades the Colonic
807 Mucus Barrier and Enhances Pathogen Susceptibility. *Cell* **167**, 1339–1353 (2016).
808 10. Johansson, M. E. V. *et al.* The inner of the two Muc2 mucin-dependent mucus layers
809 in colon is devoid of bacteria. *Proc. Natl. Acad. Sci. U. S. A.* **105**, 15064–15069 (2008).
810 11. Duncan, K., Carey-Ewend, K. & Vaishnava, S. Spatial analysis of gut microbiome
811 reveals a distinct ecological niche associated with the mucus layer. *Gut Microbes* **13**,
812 1874815 (2021).
813 12. Johansson, M. E. V., Holmén Larsson, J. M. & Hansson, G. C. The two mucus layers of
814 colon are organized by the MUC2 mucin, whereas the outer layer is a legislator of
815 host-microbial interactions. *Proc. Natl. Acad. Sci. U. S. A.* **108**, 4659–4665 (2011).
816 13. Salyers, A. A., West, S. E. H., Vercellotti, J. R. & Wilkins, T. D. Fermentation of mucins
817 and plant polysaccharides by anaerobic bacteria from the human colon. *Appl. Environ.*
818 *Microbiol.* **34**, 529–533 (1977).
819 14. Arumugam, M. *et al.* Enterotypes of the human gut microbiome. *Nature* **473**, 174–
820 180 (2011).
821 15. Xu, J. *et al.* A genomic view of the human-Bacteroides thetaiotaomicron symbiosis.
822 *Science* **299**, 2074–2076 (2003).
823 16. Sonnenburg, J. L. *et al.* Glycan foraging in vivo by an intestine-adapted bacterial
824 symbiont. *Science* **307**, 1955–1959 (2005).
825 17. Bjursell, M. K., Martens, E. C. & Gordon, J. I. Functional genomic and metabolic
826 studies of the adaptations of a prominent adult human gut symbiont, Bacteroides
827 thetaiotaomicron, to the suckling period. *J. Biol. Chem.* **281**, 36269–36279 (2006).
828 18. Morrison, D. J. & Preston, T. Formation of short chain fatty acids by the gut
829 microbiota and their impact on human metabolism. *Gut Microbes* **7**, 189–200 (2016).
830 19. Wrzosek, L. *et al.* Bacteroides thetaiotaomicron and Faecalibacterium prausnitzii
831 influence the production of mucus glycans and the development of goblet cells in the
832 colonic epithelium of a gnotobiotic model rodent. *BMC Biol.* **11**, 61 (2013).
833 20. Ríos-Covián, D. *et al.* Intestinal short chain fatty acids and their link with diet and
834 human health. *Front. Microbiol.* **7**, 185 (2016).
835 21. Louis, P. & Flint, H. J. Diversity , metabolism and microbial ecology of butyrate-
836 producing bacteria from the human large intestine. *FEMS Microbiol. Lett.* **294**, 1–8
837 (2009).

838 22. Falony, G. *et al.* In vitro kinetics of prebiotic inulin-type fructan fermentation by
839 butyrate-producing colon bacteria: implementation of online gas chromatography for
840 quantitative analysis of carbon dioxide and hydrogen gas production. *Appl. Environ.*
841 *Microbiol.* **75**, 5884–5892 (2009).
842 23. Louis, P., Duncan, S. H., Sheridan, P. O., Walker, A. W. & Flint, H. J. Microbial lactate
843 utilisation and the stability of the gut microbiome. *Gut Microbiome* **3**, e3 (2022).
844 24. Louis, P. & Flint, H. J. Formation of propionate and butyrate by the human colonic
845 microbiota. *Environ. Microbiol.* **19**, 29–41 (2017).
846 25. Duncan, S. H., Louis, P. & Flint, H. J. Lactate-Utilizing Bacteria , Isolated from Human
847 Feces , That Produce Butyrate as a Major Fermentation Product. *Appl. Environ.*
848 *Microbiol.* **70**, 5810–5817 (2004).
849 26. Duncan, S. H., Hold, G. L., Barcenilla, A., Stewart, C. S. & Flint, H. J. Roseburia
850 intestinalis sp. nov., a novel saccharolytic, butyrate-producing bacterium from human
851 faeces. *Int. J. Syst. Evol. Microbiol.* **52**, 1615–1620 (2002).
852 27. Duncan, S. H., Barcenilla, A., Stewart, C. S., Pryde, S. E. & Flint, H. J. Acetate utilization
853 and butyryl coenzyme A (CoA): Acetate-CoA transferase in butyrate-producing
854 bacteria from the human large intestine. *Appl. Environ. Microbiol.* **68**, 5186–5190
855 (2002).
856 28. D'hoe, K. *et al.* Integrated culturing, modeling and transcriptomics uncovers complex
857 interactions and emergent behavior in a three-species synthetic gut community. *Elife*
858 **7**, e37090 (2018).
859 29. Macfarlane, S., Woodmansey, E. J. & Macfarlane, G. T. Colonization of mucin by
860 human intestinal bacteria and establishment of biofilm communities in a two-stage
861 continuous culture system. *Appl. Environ. Microbiol.* **71**, 7483–7492 (2005).
862 30. Abbeele, P. Van Den *et al.* Incorporating a mucosal environment in a dynamic gut
863 model results in a more representative colonization by lactobacilli. *Microb.*
864 *Biotechnol.* **5**, 106–115 (2012).
865 31. Van Den Abbeele, P. *et al.* Butyrate-producing Clostridium cluster XIVa species
866 specifically colonize mucins in an in vitro gut model. *ISME J.* **7**, 949–961 (2013).
867 32. Van Herreweghen, F., De Paepe, K., Roume, H., Kerckhof, F. M. & Van de Wiele, T.
868 Mucin degradation niche as a driver of microbiome composition and Akkermansia
869 muciniphila abundance in a dynamic gut model is donor independent. *FEMS*

870 *Microbiol. Ecol.* **94**, fiy186 (2018).
871 33. Love, M. I., Huber, W. & Anders, S. Moderated estimation of fold change and
872 dispersion for RNA-seq data with DESeq2. *Genome Biol.* **15**, 550 (2014).
873 34. Shetty, S. A., Boeren, S., Bui, T. P. N., Smidt, H. & de Vos, W. M. Unravelling lactate-
874 acetate and sugar conversion into butyrate by intestinal Anaerobutyricum and
875 Anaerostipes species by comparative proteogenomics. *Environ. Microbiol.* **22**, 4863–
876 4875 (2020).
877 35. Martens, E. C., Chiang, H. C. & Gordon, J. I. Mucosal Glycan Foraging Enhances Fitness
878 and Transmission of a Saccharolytic Human Gut Bacterial Symbiont. *Cell Host Microbe*
879 **4**, 447–457 (2008).
880 36. Duncan, S. H., Louis, P., Thomson, J. M. & Flint, H. J. The role of pH in determining the
881 species composition of the human colonic microbiota. *Environ. Microbiol.* **11**, 2112–
882 2122 (2009).
883 37. Fischbach, M. A. & Sonnenburg, J. L. Eating For Two: How Metabolism Establishes
884 Interspecies Interactions in the Gut. *Cell Host Microbe* **10**, 336–347 (2011).
885 38. Okano, H., Hermsen, R. & Hwa, T. Hierarchical and simultaneous utilization of carbon
886 substrates: mechanistic insights, physiological roles, and ecological consequences.
887 *Curr. Opin. Microbiol.* **63**, 172–178 (2021).
888 39. Monod, J. The growth of bacteria cultures. *Annu Rev Microbiol* **3**, 371–394 (1949).
889 40. Monod, J. From Enzymatic Adaptation to Allosteric Transitions. *Science* **154**, 475–483
890 (1966).
891 41. Basan, M. *et al.* A universal trade-off between growth and lag in fluctuating
892 environments. *Nature* **584**, 470–474 (2020).
893 42. Balakrishnan, R., Silva, R. T. de, Hwa, T. & Cremer, J. Suboptimal resource allocation in
894 changing environments constrains response and growth in bacteria. *Mol. Syst. Biol.*
895 **17**, e10597 (2021).
896 43. Gray, D. A. *et al.* Extreme slow growth as alternative strategy to survive deep
897 starvation in bacteria. *Nat. Commun.* **10**, 890 (2019).
898 44. Ratzke, C., Denk, J. & Gore, J. Ecological suicide in microbes. *Nat. Ecol. Evol.* **2**, 867–
899 872 (2018).
900 45. Krulwich, T. A., Sachs, G. & Padan, E. Molecular aspects of bacterial pH sensing and
901 homeostasis. *Nat. Rev. Microbiol.* **9**, 330–343 (2011).

902 46. Marcobal, A. *et al.* Bacteroides in the Infant Gut Consume Milk Oligosaccharides via
903 Mucus-Utilization Pathways. *Cell Host Microbe* **10**, 507–514 (2011).
904 47. Brigham, C. *et al.* Sialic acid (N-acetyl neuraminic acid) utilization by Bacteroides
905 fragilis requires a novel N-acetyl mannosamine epimerase. *J. Bacteriol.* **191**, 3629–
906 3638 (2009).
907 48. Dar, D., Dar, N., Cai, L. & Newman, D. K. Spatial transcriptomics of planktonic and
908 sessile bacterial populations at single-cell resolution. *Science* **373**, 758 (2021).
909 49. Coyne, M. J. *et al.* A family of anti-Bacteroidales peptide toxins wide-spread in the
910 human gut microbiota. *Nat. Commun.* **10**, 3460 (2019).
911 50. Finkel, S. E. Long-term survival during stationary phase: Evolution and the GASP
912 phenotype. *Nat. Rev. Microbiol.* **4**, 113–120 (2006).
913 51. Zmora, N., Suez, J. & Elinav, E. You are what you eat: diet, health and the gut
914 microbiota. *Nat. Rev. Gastroenterol. Hepatol.* **16**, 35–56 (2018).
915 52. Zarrinpar, A., Chaix, A., Yooseph, S. & Panda, S. Diet and Feeding Pattern Affect the
916 Diurnal Dynamics of the Gut Microbiome. *Cell Metab.* **20**, 1006–1017 (2014).
917 53. Cinquin, C., Le Blay, G., Fliss, I. & Lacroix, C. Immobilization of infant fecal microbiota
918 and utilization in an in vitro colonic fermentation model. *Microb. Ecol.* **48**, 128–138
919 (2004).
920 54. Lamboley, L., Lacroix, C., Champagne, C. P. & Vuillemard, J. C. Continuous mixed
921 strain mesophilic lactic starter production in supplemented whey permeate medium
922 using immobilized cell technology. *Biotechnol. Bioeng.* **56**, 502–516 (1997).
923 55. Hernandez-Sanabria, E. *et al.* In vitro increased respiratory activity of selected oral
924 bacteria may explain competitive and collaborative interactions in the oral
925 microbiome. *Front. Cell. Infect. Microbiol.* **7**, 235 (2017).
926 56. Whitaker, W. R., Shepherd, E. S. & Sonnenburg, J. L. Tunable Expression Tools Enable
927 Single-Cell Strain Distinction in the Gut Microbiome. *Cell* **169**, 538-546.e12 (2017).
928 57. van de Velde, C. C. *et al.* Fast quantification of gut bacterial species in cocultures using
929 flow cytometry and supervised classification. *ISME Commun.* **2**, 40 (2022).
930 58. McInnes, L., Healy, J., Saul, N. & Großberger, L. UMAP: Uniform Manifold
931 Approximation and Projection. *J. Open Source Softw.* **3**, 861 (2018).
932 59. Chen, S., Zhou, Y., Chen, Y. & Gu, J. fastp: an ultra-fast all-in-one FASTQ preprocessor.
933 *Bioinformatics* **34**, i884–i890 (2018).

934 60. Patro, R., Duggal, G., Love, M. I., Irizarry, R. A. & Kingsford, C. Salmon provides fast
935 and bias-aware quantification of transcript expression. *Nat. Methods* **14**, 417–419
936 (2017).
937 61. Yates, A. D. *et al.* Ensembl Genomes 2022: an expanding genome resource for non-
938 vertebrates. *Nucleic Acids Res.* **50**, D996–D1003 (2022).
939 62. Olson, R. D. *et al.* Introducing the Bacterial and Viral Bioinformatics Resource Center
940 (BV-BRC): a resource combining PATRIC, IRD and ViPR. *Nucleic Acids Res.* **51**, D678–
941 D689 (2023).
942 63. Galperin, M. Y. *et al.* COG database update: focus on microbial diversity, model
943 organisms, and widespread pathogens. *Nucleic Acids Res.* **49**, D274–D281 (2021).
944 64. Kanehisa, M. Toward understanding the origin and evolution of cellular organisms.
945 *Protein Sci.* **28**, 1947–1951 (2019).
946 65. Huerta-Cepas, J. *et al.* EggNOG 5.0: A hierarchical, functionally and phylogenetically
947 annotated orthology resource based on 5090 organisms and 2502 viruses. *Nucleic*
948 *Acids Res.* **47**, D309–D314 (2019).
949 66. Cantalapiedra, C. P., Hernandez-Plaza, A., Letunic, I., Bork, P. & Huerta-Cepas, J.
950 eggNOG-mapper v2: Functional Annotation, Orthology Assignments, and Domain
951 Prediction at the Metagenomic Scale. *Mol. Biol. Evol.* **38**, 5825–5829 (2021).
952

953 ## Acknowledgements

954 We would like to thank Emma Hernandez-Sanabria, Veronica Lloréns-Rico and Jelle
955 Matthijnssens for input and support concerning bacterial transcriptomics. In addition, we
956 thank Vitor Pinheiro, Lieve Vanmellaert and Charlotte van de Velde for their help in
957 constructing the GFP tagged BT strain as well as Jeroen Raes for access to the CytoFLEX. We
958 are also grateful to Thi Thuy Duyen Nguyen, Leen Rymenans and Geert Huys of the Raes lab
959 for assistance in flow cytometry, 16S rRNA library preparation and anaerobic cultivation, as
960 well as to Raul Yhossef Tito Tadeo for processing raw 16S reads. We also thank Tobie
961 Martens from MULTIPHOTON of KU Leuven for his technical assistance in microscopy and
962 the team of Genomics Core and Metabolomics Core of KU Leuven for data acquisition. This
963 work was supported by funding from the European Research Council (ERC) under the
964 European Union's Horizon 2020 research and innovation program under grant agreement

number 801747 (EcoBox) and by KU Leuven Internal funding for Interdisciplinary Networks (ID-N) PlasticDaphnia.

Author contributions

BL, DRG and KF designed the experiments and BL and DRG carried them out. AK processed raw RNA-seq data. DG developed the kinetic model and performed simulations. KS measured metabolite concentrations. AG and KB gave advice on experimental design and interpretation. BL, DRG, KF and DG analyzed the results and BL, DRG and KF wrote the manuscript. All authors read the manuscript.

Competing interests

None

Additional information

Supplementary file 1: supplementary figures.

Supplementary file 2: description of the kinetic model.

Supplementary file 3: RNA expression data for *Bacteroides thetaiotaomicron*.

Supplementary file 4: RNA expression data for *Roseburia intestinalis*.

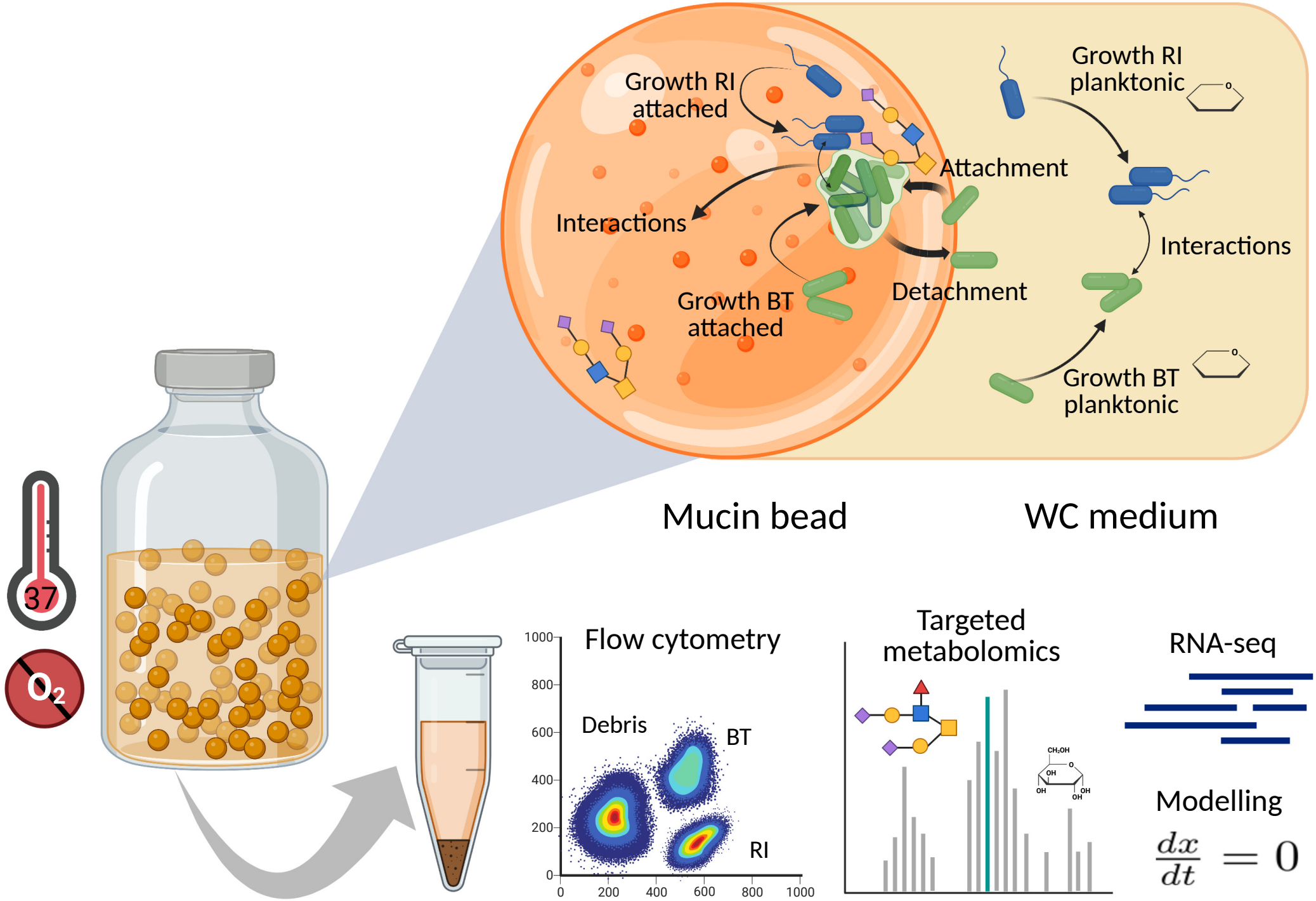
Growth RI attached
Growth RI planktonic
Attachment
Interactions
Interactions
Detachment
Growth BT attached
Growth BT planktonic
Mucin bead
WC medium
37
O2
Flow cytometry
Debris
BT
RI
1000
800
600
400
200
0
0
200
400
600
800
1000
Targeted metabolomics
RNA-seq
Modelling
$\frac{dx}{dt} = 0$

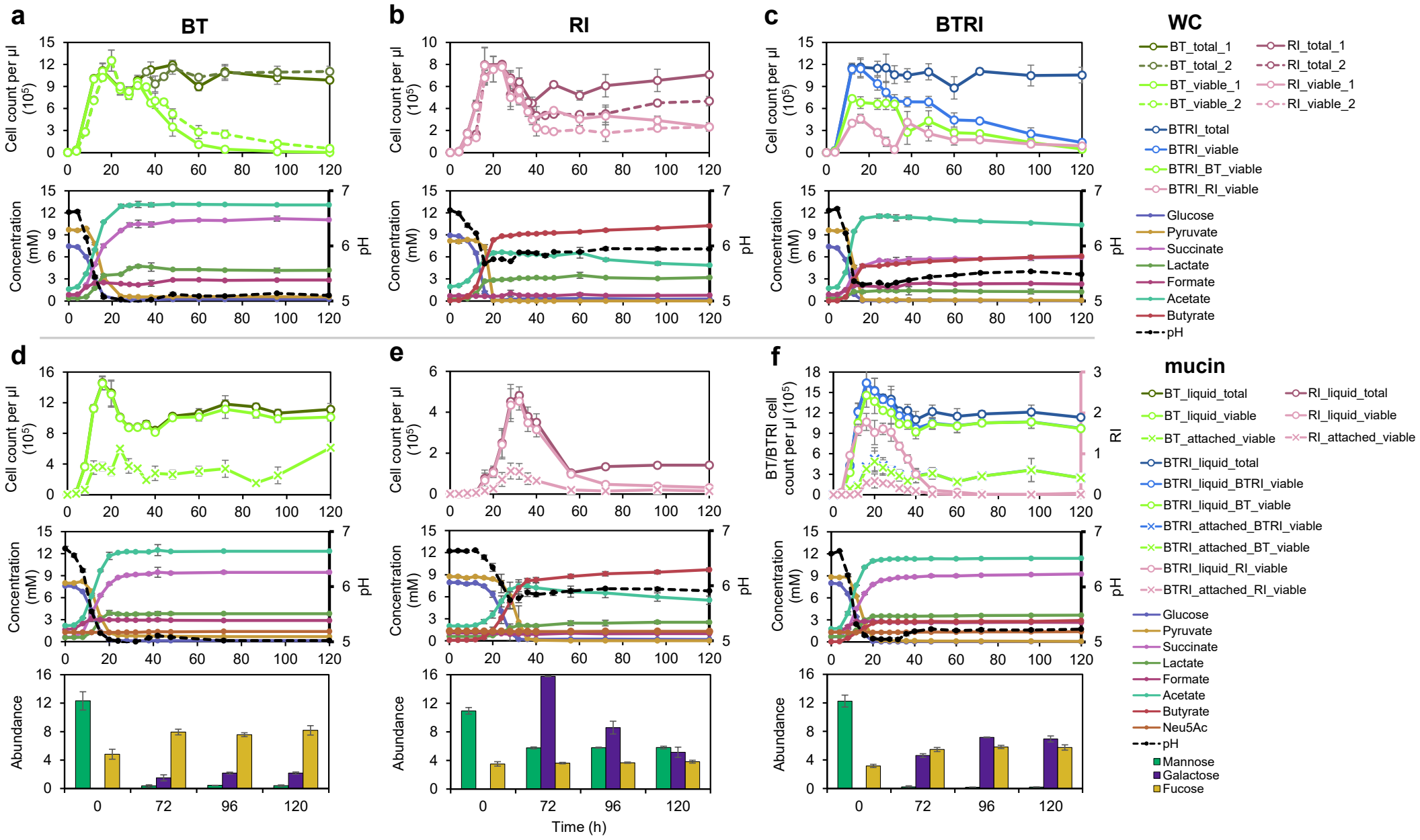
a
BT
b
RI
c
BTRI
WC
Cell count per µl (10^5)
Concentration (mM)
pH
BT_total_1
BT_total_2
BT_viable_1
BT_viable_2
RI_total_1
RI_total_2
RI_viable_1
RI_viable_2
BTRI_total
BTRI_viable
BTRI_BT_viable
BTRI_RI_viable
Glucose
Pyruvate
Succinate
Lactate
Formate
Acetate
Butyrate
pH
d
e
f
mucin
BT/BTRI cell count per µl (10^5)
RI
BT_liquid_total
BT_liquid_viable
BT_attached_viable
RI_liquid_total
RI_liquid_viable
RI_attached_viable
BTRI_liquid_total
BTRI_liquid_BTRI_viable
BTRI_liquid_BT_viable
BTRI_attached_BTRI_viable
BTRI_attached_BT_viable
BTRI_liquid_RI_viable
BTRI_attached_RI_viable
Glucose
Pyruvate
Succinate
Lactate
Formate
Acetate
Butyrate
Neu5Ac
pH
Mannose
Galactose
Fucose
Abundance
Time (h)

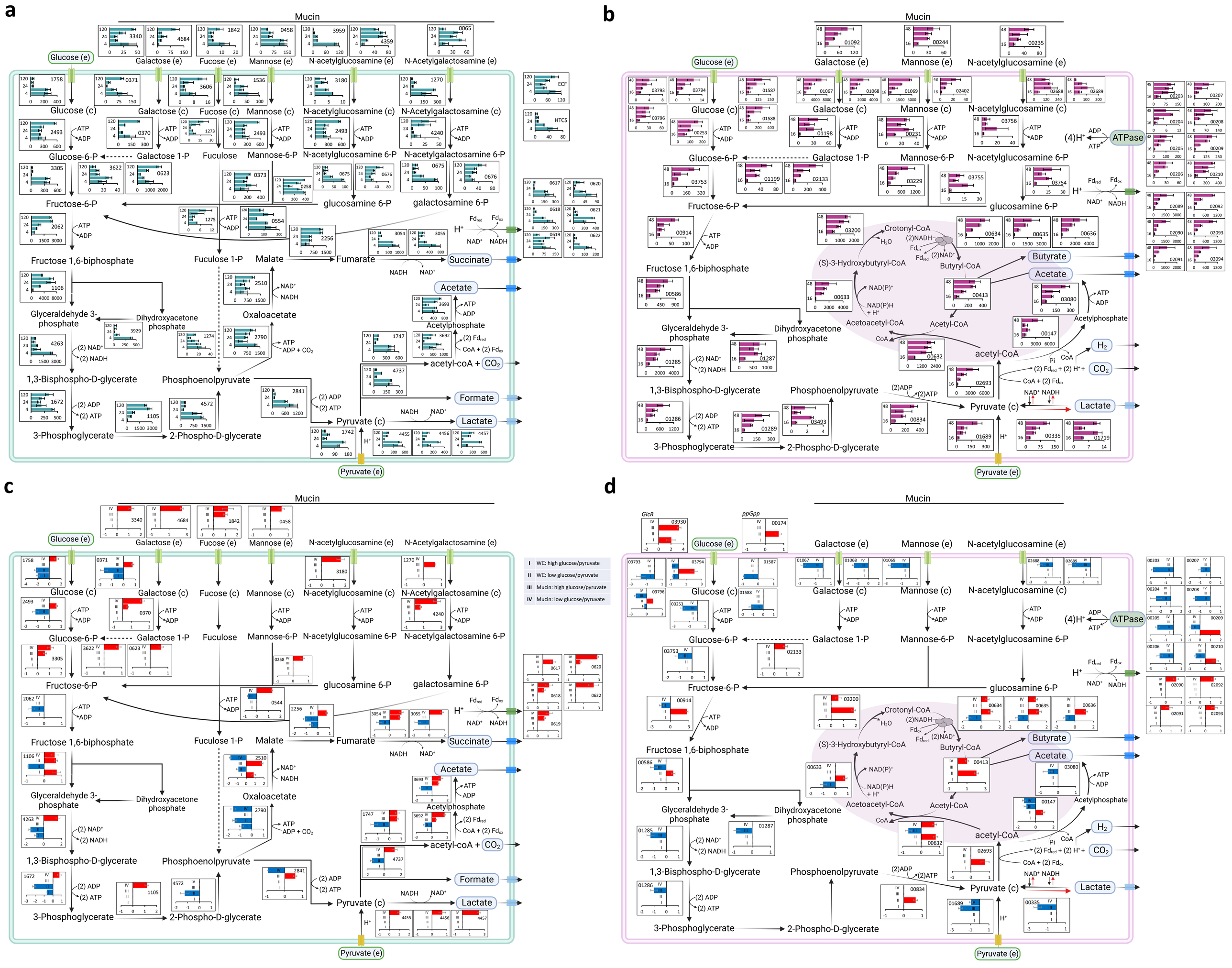
a
b
c
d
Mucin
Glucose (e)
Galactose (e)
Fucose (e)
Mannose (e)
N-acetylglucosamine (e)
N-Acetylgalactosamine (e)
Glucose (c)
Galactose (c)
Fucose (c)
Mannose (c)
N-acetylglucosamine (c)
N-Acetylgalactosamine (c)
Glucose-6-P
Galactose 1-P
Fuculose
Mannose-6-P
N-acetylglucosamine 6-P
N-acetylgalactosamine 6-P
Fructose-6-P
glucosamine 6-P
galactosamine 6-P
Fructose 1,6-biphosphate
Fuculose 1-P
Malate
Fumarate
Succinate
Acetate
Glyceraldehyde 3-phosphate
Dihydroxyacetone phosphate
Oxaloacetate
Acetylphosphate
acetyl-coA + CO2
1,3-Bisphospho-D-glycerate
Phosphoenolpyruvate
Formate
Pyruvate (c)
Lactate
3-Phosphoglycerate
2-Phospho-D-glycerate
Pyruvate (e)
ATP
ADP
ECF
HTCS
Crotonyl-CoA
(S)-3-Hydroxybutyryl-CoA
Butyryl-CoA
Butyrate
Acetoacetyl-CoA
Acetyl-CoA
Acetylphosphate
H2
CO2
(4)H+
ATPase
I WC: high glucose/pyruvate
II WC: low glucose/pyruvate
III Mucin: high glucose/pyruvate
IV Mucin: low glucose/pyruvate
GlcR
ppGpp

a

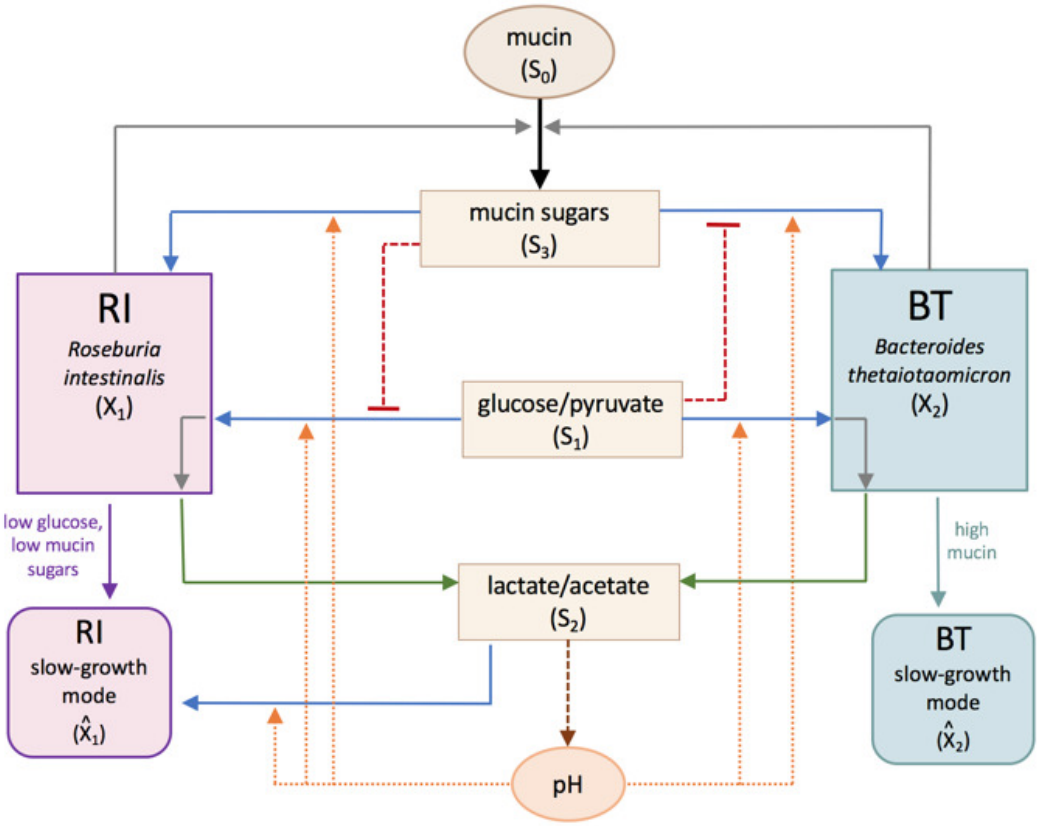
mucin
(S_0)
mucin sugars
(S_3)
RI
Roseburia intestinalis
(X_1)
BT
Bacteroides thetaiotaomicron
(X_2)
glucose/pyruvate
(S_1)
low glucose, low mucin sugars
high mucin
lactate/acetate
(S_2)
RI
slow-growth mode
($\hat{X}_1$)
BT
slow-growth mode
($\hat{X}_2$)
pH

b

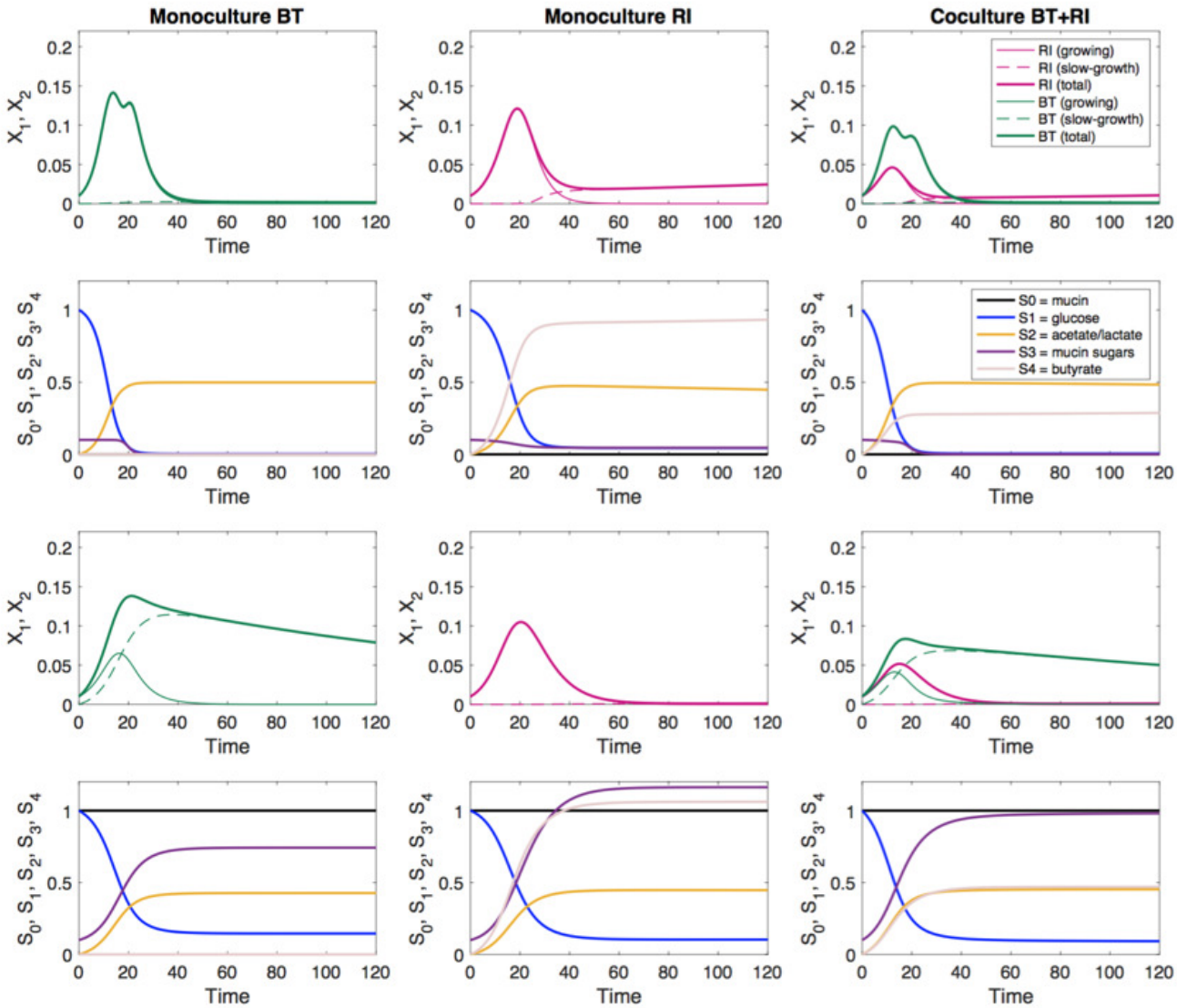
Monoculture BT
Monoculture RI
Coculture BT+RI
X_1, X_2
S_0, S_1, S_2, S_3, S_4
Time
RI (growing)
RI (slow-growth)
RI (total)
BT (growing)
BT (slow-growth)
BT (total)
S0 = mucin
S1 = glucose
S2 = acetate/lactate
S3 = mucin sugars
S4 = butyrate

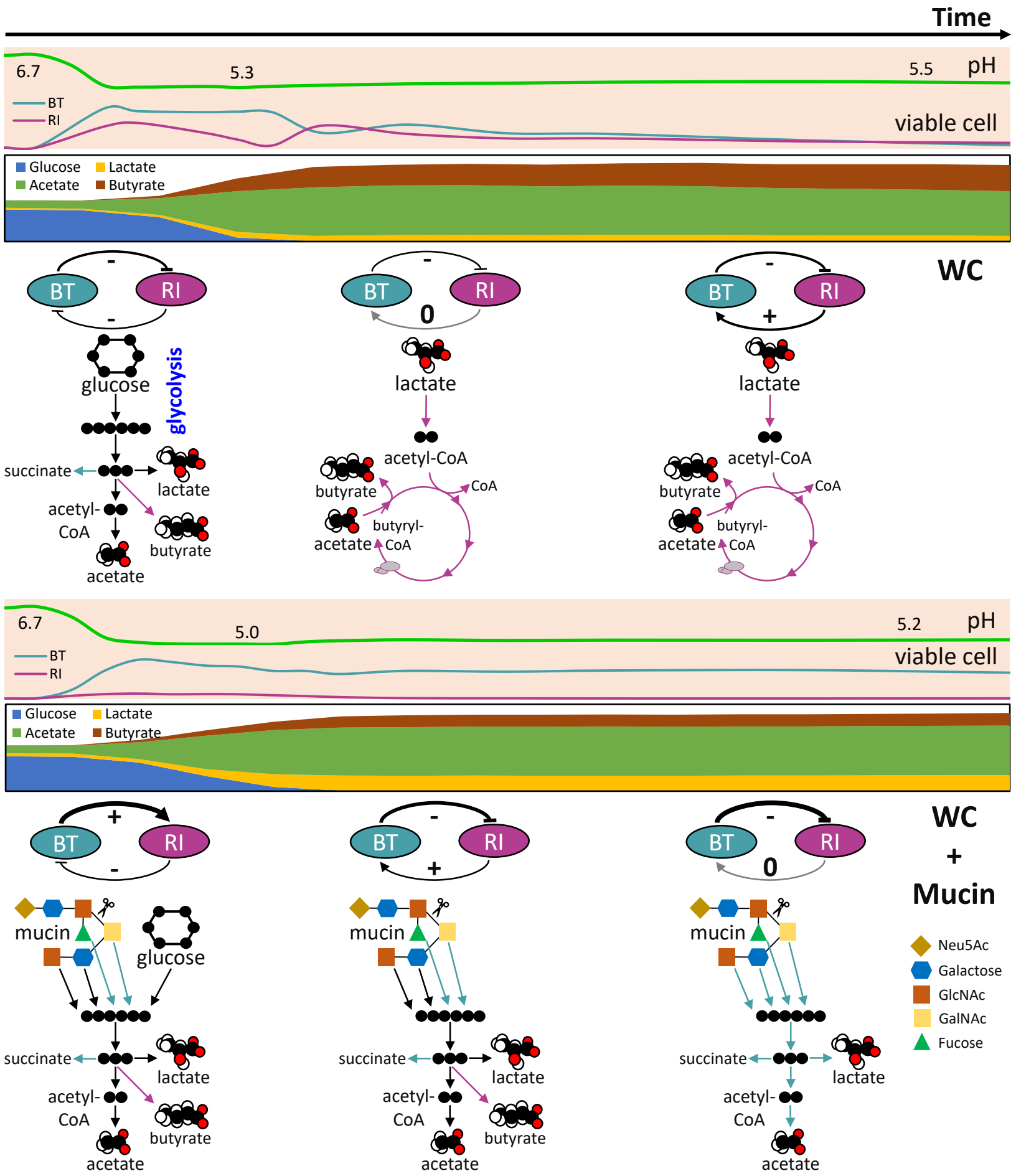

Time
6.7
5.3
5.5
pH
BT
RI
viable cell
Glucose
Lactate
Acetate
Butyrate
WC
BT
RI
glucose
glycolysis
succinate
lactate
acetyl-CoA
butyrate
acetate
0
lactate
acetyl-CoA
butyrate
CoA
acetate
butyryl-CoA
+
6.7
5.0
5.2
pH
BT
RI
viable cell
Glucose
Lactate
Acetate
Butyrate
WC
+
Mucin
mucin
glucose
succinate
lactate
acetyl-CoA
butyrate
acetate
0
Neu5Ac
Galactose
GlcNAc
GalNAc
Fucose